Bio-Design and Manufacturing (2026) 9:514–538
https://doi.org/10.1631/bdm.2500128

RESEARCH ARTICLE

Comparative analysis of the safety and efficacy of 3D-bioprinted constructs embedded with human mesenchymal stem cells for bone regeneration

Jung Ho Jeon[1] · Jae-Seok Kim[3] · Hun-Jin Jeong[3,5] · Eun Chae Kim[3] · Hyeon Jun Yoon[8] · Hye Won Kim[9] · Eunju Hong[8] · Man Soo Kim[10] · Jung Yeon Lim[2] · Minho Lee[8] · Seung-Jae Lee[3,4,6,7] · Sung Won Kim[2]

Received: 17 March 2025 / Accepted: 31 August 2025

Abstract

Advanced therapy medicinal products are biological products that require rigorous long-term monitoring of safety and efficacy due to their sustained effects. The development of tissue-engineered products demands careful consideration of tissue-specific properties, surgical requirements, biomaterial compatibility, host tissue integration, and potential immune responses. In this study, we developed and evaluated the safety and efficacy of 3D-bioprinted constructs containing cells for bone regeneration in preclinical models. Three types of human mesenchymal stem cells (bone marrow-derived, adipose-derived, and nasal turbinate-derived) were combined with varying concentrations of collagen and polycaprolactone. Safety assessments included comprehensive tumorigenicity evaluations involving cell viability assays, protein quantification, and whole-genome sequencing under multiple conditions to confirm genetic stability and mitigate tumorigenic risks. Short-term toxicity was evaluated by subcutaneous implantation in nude mice, with blood and serum analyses confirming the absence of acute toxicity or histological abnormalities in major organs. Efficacy studies in rabbits exhibited safety through post-transplantation analyses, with 6-month tissue analyses showing significantly elevated expression of osteopontin and runt-related transcription factor 2 (RUNX2) proteins in constructs containing human nasal turbinate-derived mesenchymal stem cells, indicating successful tissue integration and bone-specific marker expression. Long-term follow-up confirmed construct integrity and sustained bone formation. These findings highlight the importance of comprehensive safety and efficacy evaluations across cell types and construct compositions in the development of 3D-bioprinted constructs for bone regeneration. This study establishes a systematic framework for material selection and validation in preclinical stages, providing a foundation for future clinical applications in regenerative medicine and tissue engineering.

✉ Minho Lee
MinhoLee@dgu.edu

✉ Seung-Jae Lee
sjlee411@wku.ac.kr

✉ Sung Won Kim
kswent@catholic.ac.kr

[1] Department of Biomedicine and Health Science, College of Medicine, The Catholic University of Korea, Seoul 06591, Republic of Korea

[2] Department of Otolaryngology-Head and Neck Surgery, Seoul St. Mary's Hospital, College of Medicine, The Catholic University of Korea, Seoul 06591, Republic of Korea

[3] Department of Mechanical Engineering, Wonkwang University, Iksan 54538, Republic of Korea

[4] Division of Mechanical Engineering, Wonkwang University, Iksan 54538, Republic of Korea

[5] College of Dental Medicine, Columbia University Irving Medical Center, New York, NY 10032, USA

[6] Advanced Bio-Convergence Research Center, Wonkwang University, Iksan 54538, Republic of Korea

[7] MECHABIO Group, Wonkwang University, Iksan 54538, Republic of Korea

[8] Department of Life Science, Dongguk University, Seoul 04620, Republic of Korea

[9] Department of Industrial Pharmacy, Dongguk University, Seoul 04620, Republic of Korea

[10] Department of Orthopedic Surgery, Seoul St. Mary's Hospital, College of Medicine, The Catholic University of Korea, Seoul 06591, Republic of Korea

Graphical abstract

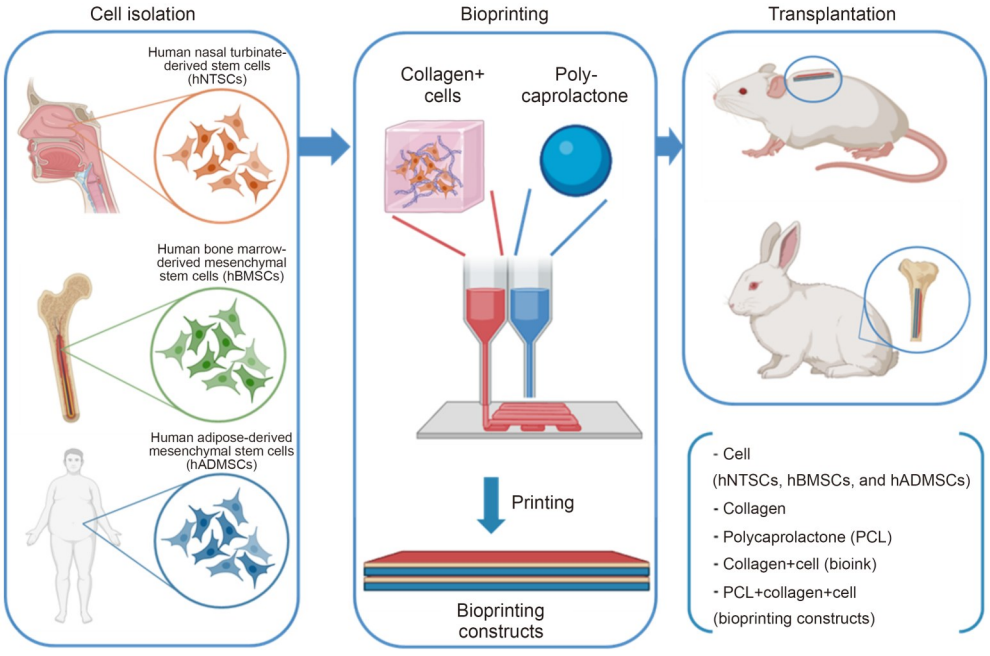

Keywords Mesenchymal stem cells · 3D printing · Bioprinting · Acute toxicity test · Transplantation

1 Introduction

Various diseases affect tissues and organs through the degeneration or dysfunction of specific cell types, leading to progressive deterioration and loss of function [1]. Regenerative medicine offers promising approaches to addressing such challenging pathologies [1]. In recent years, numerous clinical trials have targeted a wide range of diseases. Current strategies focus on optimizing therapy by selecting the most effective material compositions, ensuring scalability in production, and expediting clinical translation [2].

Advanced therapy medicinal products (ATMPs) include cell therapy products, gene therapy products, and tissue-engineered products [3]. Compared to conventional medicines, ATMPs present unique challenges due to their cell and tissue origins and the complexity of manufacturing processes that rely on innovative technologies [4]. The development of these products is inherently complex, costly, and demanding due to these characteristics, which are further compounded by the therapeutic targeting of rare diseases or those without existing treatment options. Key challenges include manufacturing constraints, nonclinical development planning, clinical trial design, marketing authorization (MA), and post-MA surveillance [5].

Tissue engineering has recently emerged as a promising approach in regenerative therapy, combining three-dimensional (3D) degradable compounds with various cell types to form matrices for cell-based therapies [6]. Cell-containing 3D bioprinting incorporates diverse sources, including patient-derived tissues, human cadavers, and fetal tissue materials. Cells obtained from adult tissues are typically harvested directly from patients and then expanded under sterile conditions to generate sufficient quantities for therapeutic use [7]. From an industrial perspective, autologous cell-based therapies simplify the manufacturing process; however, meeting large-scale supply demands remains a significant challenge [8]. To address this limitation, donor-derived cells are evaluated for histocompatibility and genetic safety before selection for product development. This also applies to the materials used in the structural components of 3D-bioprinted constructs.

Stem cells intended for therapeutic use possess properties that distinguish them from differentiated adult cells [9]. The therapeutic paradigm has evolved toward the direct administration of living stem cells to patients, leveraging their self-renewal capacity and multipotent properties [10]. Various strategies have been developed to obtain stem cells as candidate therapeutic agents for disease treatment. However, methodological and ethical challenges continue to affect stem cell production [11]. Stem cells commonly used to circumvent these challenges include human bone marrow-derived mesenchymal stem cells (hBMSCs), human adipose-derived mesenchymal stem cells (hADMSCs), and human nasal turbinate-derived stem cells (hNTSCs).

These mesenchymal stem cells (MSCs) can differentiate into multiple tissue-specific cell types, and the therapeutic efficacy of stem cell transplantation into damaged tissues may vary depending on the cell quantity [9, 12]. For clinical applications, significant efforts have been made to produce large numbers of stem cells under laboratory conditions. Such stem cells can be used in tissue engineering to restore or replace damaged tissues. Tissue engineering involves strategies for tissue regeneration and organ repair that employ suitable substrates for cell attachment, proliferation, and differentiation in combination with stem or adult cells, as well as regulatory factors that influence cellular growth and specialization [13]. The substrates are derived from various biological sources, most commonly biodegradable materials such as collagen and polycaprolactone (PCL) [14].

In tissue engineering and regenerative medicine, 3D bioprinting is used to fabricate a wide range of biological structures. By precisely controlling 3D patterns using biomaterials, including biodegradable compounds, tissues can be reproduced by stacking layers to form complex structures [15]. Imaging techniques such as X-ray, magnetic resonance imaging, and computed tomography are used to confirm that the fabricated constructs accurately replicate patient tissues, enabling the production of identical structures. Through the integration of cells with structural materials, this fabrication method allows the creation of artificial biological tissues and organs designed for therapeutic applications, replicating both the structural and chemical properties of human organs and tissues [16].

Extensive experiments are required to prepare 3D-bioprinted tissues for clinical trials. Previous studies using novel materials and cells that can replace human tissues have primarily examined the characteristics and similarities of artificial tissues; however, the studies necessary to support clinical translation have not yet been completed [17]. Showing both efficacy and safety in accordance with regulatory requirements is essential for clinical trials involving 3D-bioprinted tissue constructs. Given that these constructs contain stem cells, evaluations must address cellular properties and structural characteristics, unlike constructs composed solely of biomaterials [18]. Additionally, careful assessment of tumorigenic potential following transplantation and the risk of genetic mutations arising from different culture methods and environments is crucial; studies confirming these concerns should be conducted. Posttransplant toxicity must also be evaluated, and the corresponding efficacy results should be incorporated [19].

The current evaluation of tissue-engineered medical products follows established international standards, including ISO 21560: 2020 for general requirements, the ISO 10993 series for biological evaluation, and ASTM F2721 for preclinical assessment. Clinical translation additionally requires compliance with regulatory frameworks, such as the US Food and Drug Administration guidance for bone graft substitutes and the European Medicines Agency guidelines for advanced therapy medicinal products.

However, these standards provide limited guidance on the comprehensive genetic safety assessment of cell-laden constructs. To address this gap, this study incorporated extensive genomic analysis alongside conventional evaluation parameters, recognizing that genomic stability is a crucial factor in ensuring therapeutic safety.

Specifically, we examined the safety and efficacy evaluation methods appropriate for preclinical studies intended to support clinical research across multiple diseases. Using several types of clinically applied stem cells and materials incorporated into 3D-bioprinted constructs, we aimed to identify condition-dependent changes and propose essential methodological considerations for preclinical research.

2 Materials and methods

2.1 Isolation and culture

The cell culture protocol used in this study was adapted from previously validated methods for isolating and maintaining hNTSCs, as reported in earlier studies [20–22]. These protocols were selected due to their reproducibility, ability to preserve multipotency, and minimal donor-site morbidity. Hwang et al. [20] first established the feasibility of isolating multipotent MSCs from inferior turbinate tissue and confirmed their trilineage differentiation potential, as well as the expression of MSC-specific surface markers (CD29, CD73, CD90) in the absence of hematopoietic markers (CD14, CD19, CD34, HLA-DR). Follow-up studies have further validated that key hNTSC characteristics, including proliferative capacity and osteogenic differentiation potential, are not significantly affected by donor age [21] or turbinate size [22], supporting their reliability as a consistent MSC source. These findings provide the rationale for applying this protocol in the present study. To ensure the identity and quality of the cultured cells, fluorescence-activated cell sorting was performed to confirm the expression of canonical MSC markers before experimental use. The hNTSCs were isolated from the nasal inferior turbinate tissue of a patient during partial turbinectomy. The tissue was washed with saline and Dulbecco's phosphate-buffered saline (PBS; Thermo Fisher Scientific, Waltham, MA, USA, 14190144) supplemented with gentamicin (Thermo Fisher Scientific, 15710064) and antibiotic-antimycotic solution (Thermo Fisher Scientific, 15240062).

The obtained tissue was cut into 1-mm^3 pieces, plated in a culture dish, and covered with a sterilized glass coverslip. The tissue was incubated in alpha-minimum essential medium (Thermo Fisher Scientific, 12492013) supplemented

with 1% (volume fraction) penicillin–streptomycin (Thermo Fisher Scientific, 15140122) and 10% (volume fraction) fetal bovine serum (Thermo Fisher Scientific, 16000044). Incubation was performed at 37 °C in a humidified atmosphere containing 5% (volume fraction) CO_2. The culture medium was replaced every 2–3 d for three weeks. Afterward, the coverslip was removed, and the adherent cells were harvested using a 0.25% trypsin solution with 1 mmol/L ethylene diamine tetraacetic acid (EDTA, Thermo Fisher Scientific, 15400054). Similar to other MSC types, hNTSCs were expanded through three to four passages before use in the experiments. hBMSCs (catalog No. C-12974, batch No. 475Z011.3) and hADMSCs (catalog No. C-12977, batch No. 485Z035) were purchased from PromoCell (Heidelberg, Germany). Both cell types were cultured in Mesenchymal Stem Cell Growth Medium 2 (PromoCell, C-28009), including the manufacturer-provided supplement mix. Cells were incubated at 37 °C in a humidified atmosphere containing 5% (volume fraction) CO_2 and expanded through three to four passages before experimental use.

2.2 Preparation of cell-laden collagen bioink

To prepare the cell-laden collagen bioink, type I collagen (UBIOSIS, Seongnam, Republic of Korea, TL330) at 3% (30 g/L) was obtained. Cell suspensions were prepared from each cell source by detaching hNTSCs, hBMSCs, and hADMSCs from their culture plates. Each suspension was then mixed with collagen solutions at final concentrations of 2.7% (27 g/L) and 1.1% (11 g/L). The total cell density was adjusted to 10^6 cells/mL. Before bioprinting, the rheological properties of the 1.1% and 2.7% collagen-based bioinks were assessed using a rotational rheometer (DHR10, TA Instruments, USA) to verify their suitability for extrusion-based 3D bioprinting.

2.3 3D printing of cell-laden constructs

PCL (M_w=73,000; Resomer® C209; Evonik Industries, Germany) was used to fabricate the 3D constructs as previously described. PCL pellets were loaded into a 10 mL stainless steel syringe (SS10; U-Jin Tech., Siheung, Republic of Korea) and melted at 90 °C. The molten PCL was extruded through a precision nozzle under a pneumatic pressure of approximately 550 kPa. For the acute toxicity model, a 200 μm nozzle (PRN0.2; U-Jin Tech.) with a feed rate of 430 mm/min was used to produce scaffolds measuring 5 mm×5 mm×1.6 mm (Fig. S3a in the supplementary information). To reduce tissue irritation during subcutaneous implantation, the scaffold corners were beveled at 45°. For the tibial defect model, a 150 μm nozzle (PRN0.15; U-Jin Tech.) and a feed rate of 210 mm/min were used to fabricate scaffolds measuring 4.5 mm×4.5 mm×1 mm (Fig. S3b in the supplementary information). All constructs were fabricated using a custom-built, multi-head extrusion-based bioprinting system designed for laboratory-scale applications (Fig. S1 in the supplementary information). Cell-laden collagen bioinks at 1.1% (11 g/L) and 2.7% (27 g/L) were maintained at 4 °C and dispensed into the open pores of the printed PCL scaffolds using a 1 mL syringe. In this system, the PCL framework provides mechanical support and spatial stability, while the collagen hydrogel occupies the internal voids, creating a cell-friendly microenvironment. Unlike co-printing in alternating layers, the two materials were integrated spatially, maintaining distinct structural and biological functions (Fig. S2 in the supplementary information).

2.4 Analysis of the mechanical properties of 3D constructs

The mechanical properties of the 3D-bioprinted constructs were evaluated using uniaxial compression testing on a universal testing machine (Model E42, MTS, Germany) equipped with a 5.0 kN load cell. Compression tests were conducted on eight constructs per group (n=8) for the acute toxicity and tibial defect models. Constructs were compressed at a constant crosshead speed of 1 mm/min until they reached 40% strain. Stress–strain curves were generated, and the elastic modulus (E) was calculated from the linear region, typically between 0% and 10% strain. These measurements were used to assess the mechanical suitability of the constructs for bone tissue engineering applications.

2.5 Cell viability and growth in cultures and constructs

The viability of hNTSCs, hBMSCs, and hADMSCs within each printed construct was assessed on Days 1, 3, and 7 using a LIVE/DEAD Viability/Cytotoxicity Kit (Invitrogen, Thermo Fisher Scientific, L3224). Constructs containing MSCs were briefly washed with PBS and treated with calcein acetoxymethyl ester (calcein AM) and ethidium homodimer, followed by incubation for 30 min at 37 °C in a 5% (volume fraction) CO_2 incubator. Stained cells were observed using a confocal laser scanning microscope (LSM 510 Meta; Carl Zeiss Meditec AG, Jena, Germany). Cell proliferation in cultures and constructs was measured at the designated time points using a WST-8 Assay Kit (DAEILLAB Co., Seoul, Republic of Korea; http://www.daeillab.co.kr, EZ-3000). For each sample, the WST-8 solution was diluted at 1:10 with a culture medium relative to the total culture volume. Samples were incubated in the diluted WST-8 solution for 30 min to ensure complete coverage, and absorbance was measured at 450 nm using a microplate reader (Molecular Devices, Sunnyvale, CA, USA).

2.6 Cytokine antibody array

Cytokine protein levels in conditioned media from hNTSCs, hBMSCs, and hADMSCs were measured using a Human Cytokine Array C-5 (RayBiotech, Norcross, GA, USA, AAH-CYT-5; Table S1 in the supplementary information) according to the manufacturer's instructions. Cytokine array membranes were first blocked with blocking buffer at 23 °C for 30 min and then incubated with 1 mL of conditioned media derived from human mesenchymal stem cells (hMSCs) at 4 °C overnight. Membranes were subsequently washed three times with wash buffer I and twice with wash buffer II at room temperature for 5 min per wash. The membranes were incubated with biotin-conjugated antibodies at room temperature for 2 h, followed by incubation with horseradish peroxidase-conjugated streptavidin at room temperature for 2 h. Finally, the membranes were treated with detection buffer for 2 min. Array images were scanned using ImageJ (National Institutes of Health, Bethesda, MD, USA), and the optical density of each spot was quantified by measuring the mean gray value.

2.7 3D bioprinting process and somatic mutation analysis

Whole-genome sequencing (WGS) data were obtained from 24 samples, including constructs subjected to different stages of the 3D bioprinting process and untreated controls. Libraries were prepared using the Illumina TruSeq Nano DNA Sample Preparation Kit. Genomic DNA (gDNA) was extracted using the QIAamp® DNA Mini Kit (Qiagen, Netherlands) with the following modifications: 3D bioprinted constructs were lysed using 350 μL of buffer ATL. Lysed meningioma was treated with 1.5 mg/mL proteinase K at 56 °C for 1 h with brief vortexing every 15 min. The digested mixture was cleared by centrifugation and subsequently treated with 2 mg/mL RNase A at room temperature for 2 min. Buffer AL (385 μL) was added, briefly vortexed, and incubated at 70 °C for 10 min, followed by the addition of 385 μL of 100% ethanol. Samples were centrifuged at 12,000 r/min for 1 min, transferred to spin columns, and then washed with buffers AW1 and AW2. Residual buffer was removed through a 1-min spin at 12,000 r/min. Nucleotides were eluted from the columns in two separate 75 μL DNase/RNase-free water elutions, with a 5-min column incubation. Extracted gDNA was immediately snap-frozen and stored at −80 °C. The 3D bioprinting workflow consists of three steps: treatment with collagen, application of PCL, and a one-week incubation period. Each of the 24 samples represented a unique condition, defined by three cell types, three bioprinting stages plus control status, and two collagen concentrations (1.1% or 2.7%). Notably, groups treated with 1.1% and 2.7% collagen were derived from different control cell populations. Using these raw data, somatic variant and copy number variation (CNV) analyses were performed with default parameters, unless otherwise specified.

Quality control of raw sequencing reads was performed using FastQC (v0.12.1) and MultiQC (v1.17) [23]. Adapter sequences from Illumina TruSeq were removed using Trimmomatic (v0.39) [24], which employs the built-in TruSeq3-PE-2.fa file. Low-quality regions were also trimmed with the same tool. Processed reads were aligned to the latest human reference genome, GRCh38. p14, from the National Center for Biotechnology Information (NCBI) using Burrows-Wheeler Aligner with Maximal Exact Matches (BWA-MEM, v0.7.17) [25]. After alignment, base recalibration, variant calling, and variant filtering were conducted using the Genomic Analysis Toolkit (GATK, v4.4.0.0) [26] according to the GATK Best Practices workflow. Duplicate reads were removed using MarkDuplicates during the generation of the binary sequence alignment map (BAM) files.

The BAM files were further recalibrated using BaseRecalibrator and ApplyBQSR, and a panel of normals (PoN) was generated to filter false-positive variants. Variant calling was conducted using Mutect2 [27]. Unexpected incompatibilities arose between the BAM and PoN files when used as inputs for downstream GATK tools, which require chromosome names in the format used by the University of California, Santa Cruz (UCSC), USA. To resolve this, chromosome names were converted from NCBI to UCSC format using chromToUCSC (https://hgdownload.soe.ucsc.edu/admin/exe/linux.x86_64/chromToUcsc) and BCFtools (v1.18) [28]. Corresponding chromosome annotation files were obtained from UCSC (https://hgdownload.cse.ucsc.edu/goldenpath/hg38/bigZips/p14/hg38.p14.chromAlias.txt) and NCBI (https://www.ncbi.nlm.nih.gov/datasets/genome/GCF_000001405.40). Contaminated variants were filtered using CalculateContamination and FilterMutectCalls. The final variant dataset was annotated using Funcotator, linking mutations with human diseases based on databases such as ClinVar and the COSMIC Cancer Gene Census (CGC). ANNOVAR [29] was used to further evaluate the potential risks associated with each variant.

Variant data were analyzed to determine the total number of variants, which were classified according to their genomic loci and their potential impact on protein sequences. Annotations from ClinVar and CGC were assessed by processing the data into mutation annotation format (MAF) in the R package maftools (v2.18.0) [30]. Synonymous mutations were identified, including those located in the 5′ flanking region, introns, silent loci, intergenic regions, and the 5′- and 3′-untranslated regions. Nonsynonymous variants were categorized into five types: missense, nonsense, splice site, frameshift deletions/insertions, and in-frame deletions/insertions. CGC and ClinVar annotations were obtained from

the MAF file. Somatic mutation profiles were visualized in the R package ggplot2 (v3.5.1) [31], ggpubr (v0.6.0) [32], and ggVennDiagram (v1.2.2) [33].

CNV analysis followed the same workflow through the ApplyBQSR step. The GATK-recommended method was then applied following the Best Practices guidelines for sensitive detection of copy ratio alterations and allelic segments. CNV profiles were visualized as scatter plots for individual samples and as a heatmap for all samples, with genomic loci on the *x*-axis. The CNV analysis utilized the recommended pipeline from CNVkit [34] with the batch command and the method set to "wgs" for WGS data. Visualization of CNV profiles was performed using heatmap plotting commands in the CNVkit.

2.8 Implantation of 3D-bioprinted cell constructs in nude mice

Male BALB/c nude mice (six weeks old, Orient Bio Co., Seongnam-si, Republic of Korea; n=5 per group, total n=40) were assigned to eight experimental groups: 1.1% collagen-based constructs without cells (PCL/collagen, n=5); 1.1% collagen-based constructs containing hNTSCs (bioprinted-hNTSCs, n=5), hBMSCs (bioprinted-hBMSCs, n=5), or hADMSCs (bioprinted-hADMSCs, n=5); 2.7% collagen-based constructs without cells (n=5); and 2.7% collagen-based constructs containing the same cell types (each n=5). Mice were anesthetized with Zoletil (30 mg/kg; Virbac Laboratory, Carros, France) and Xylazine (10 mg/kg; Rompun, Bayer, Mexico City, Mexico). Each 3D-bioprinted construct measured 5 mm in length, 5 mm in width, and 1.6 mm in height, and was implanted aseptically into the dorsal subcutaneous region of each mouse, approximately 2 cm caudal to the occipital region and slightly to the right of the midline to avoid the vertebral column. One construct was implanted per animal. Constructs were placed with minimal pressure to maintain position without the use of adhesives or sutures. Mice were euthanized at 1, 7, and 14 d post-implantation, and the implanted constructs were harvested. Samples were fixed in 4% paraformaldehyde, dehydrated in graded ethanol, cleared, and embedded in paraffin wax. Tissue processing and embedding were conducted according to the protocol described by Yun et al. [35].

2.9 Tibial defect rabbit model and 3D cell-printed construct implantation

To evaluate the therapeutic efficacy of 3D-bioprinted constructs containing hNTSCs, hBMSCs, and hADMSCs in vivo, male New Zealand White rabbits (approximately 3.5 kg; Raonbio Co., Yongin-si, Republic of Korea; n= 5 per group, total n=20) were assigned to four experimental groups: 3D constructs without cells (PCL/collagen, n=5), or 3D constructs containing hNTSCs, hBMSCs, or hADMSCs (each n=5). Rabbits were anesthetized using intramuscular injections of Zoletil (15 mg/kg) and Xylazine (5 mg/kg). After shaving and disinfecting the surgical site, a medial incision was made to access the tibial surface. Soft tissue and periosteum were retracted to access the tibial metaphysis. A monocortical bone defect (diameter: 4.5 mm; depth: 1 mm) was created on the anteromedial aspect of the tibia using a low-speed rotary burr, carefully avoiding the medial collateral ligament. A preconditioned 3D-bioprinted construct (diameter: 4.5 mm; height: 1 mm) was implanted into the defect site of each animal according to group assignment. Subcutaneous tissue and skin were closed using absorbable 4-0 Vicryl sutures (Ethicon, Somerville, NJ, USA). Postoperative care included daily subcutaneous injections of gentamicin (4 mg/kg) and ketoprofen (3 mg/kg) for 7 d, starting 1 d before surgery. All procedures adhered to institutional guidelines for animal care and use. Harvested samples were fixed in 10% formalin (Merck Millipore, Burlington, MA, USA, HT501128), decalcified in 0.5 mol/L EDTA solution (Dynebio, Seoul, Republic of Korea, CBE3011) at room temperature for six weeks with regular solution changes, dehydrated through a graded ethanol series, cleared in xylene, and embedded in paraffin wax for histological analysis.

2.10 Blood sampling and analysis

Blood samples from anesthetized mice were collected from the inferior vena cava on the day of sacrifice. Samples were drawn from two types of tubes: one without additives for biochemical analysis and the other containing EDTA for hematologic analysis. Collected samples were gently mixed, placed in a thermobox, and transported to the laboratory. Hematologic parameters were measured, and following centrifugation (3 min, 3000 r/min, 24 °C), plasma and serum were stored at −80 °C.

For rabbits, blood samples were collected from the marginal ear vein of restrained rabbits, with one person holding the animal and another collecting the blood. Rabbits were placed in restraining bags that exposed only the ears. Blood was collected in the same two types of tubes used for mice. Samples were transported in a thermobox, analyzed in the laboratory, and stored at −80 °C after centrifugation.

2.11 Histological analysis

Paraffin-embedded tissue sections (2.5 μm thickness) were deparaffinized using xylene and subsequently rehydrated through a series of graded ethanol solutions. The sections were stained with a hematoxylin and eosin (H&E) staining kit (Abcam, Cambridge, UK, ab245880). Additional sections were stained using a Trichrome Stain Kit (Abcam, ab150686).

2.12 Immunofluorescence analysis

Before immunofluorescence staining, tissue sections were deparaffinized using xylene and ethanol and washed with PBS. Antigen retrieval was performed using a proteinase K solution (Abcam, ab64220), followed by blocking with 1% (10 g/L) normal goat serum (Vector Laboratories, Inc., Plain City, OH, USA, S-1000-20). Sections were then incubated with primary antibodies: anti-osteopontin (OPN; 1:300, Abcam, ab214050) or anti-runt-related transcription factor 2 (RUNX2; 1:300, Abcam, ab192256). Secondary staining was performed using goat anti-rabbit or anti-mouse Alexa Fluor 488 (Thermo Fisher Scientific, A-11001) or 546 (Thermo Fisher Scientific, A-11030) antibodies at a 1:1000 dilution. Nuclei were labeled with 4′,6-diamidino-2-phenylindole (DAPI; Thermo Fisher Scientific, 62248), and fluorescence images were acquired using a Zeiss LSM800 confocal microscope (Carl Zeiss Meditec, Germany).

2.13 Quantification and statistical analysis

Statistical analyses were performed using a two-way analysis of variance (ANOVA) or Student's *t*-test in Prism software (v8.0; GraphPad Software, San Diego, CA, USA). Data from at least three independent experiments are presented as mean±standard deviation (SD) or mean±standard error of the mean (SEM). Tukey's post hoc ANOVA test was used for multiple comparisons to assess statistically significant differences among groups, while the Student's *t*-test was applied to compare the two samples. A *p*-value of <0.05 was considered statistically significant. Immunohistochemical staining was examined using a slide scanner for digital pathology (SCN400, Leica, Wetzlar, Germany) under 100× or 200× objective lenses. Immunofluorescence was observed using a confocal microscope, and fluorescence images were analyzed using MetaMorph software (v7.5; Molecular Devices, LLC, San Jose, CA, USA).

3 Results

3.1 Comparison of 3D-bioprinted construct characteristics

We employed three commonly used stem cell types for cell therapy: hBMSCs [36], hADMSCs [37], and hNTSCs [38, 39]. Medical PCL was used as the bioprinting material, and collagen served as the cell-supporting matrix, both of which have been shown to be safe in vitro and in vivo [40–42]. The cells were embedded in two collagen concentrations to fabricate 3D-bioprinted constructs (Fig. 1a). The biological characteristics of the constructs were compared by monitoring cell proliferation under each condition. Proliferation was observed over time in all groups, including hNTSCs, hBMSCs, and hADMSCs (Figs. 1b and 1c). Quantitative analysis confirmed normal proliferation under 1.1% and 2.7% collagen treatments for each hMSC type (Fig. 1b). The hNTSCs showed a significant increase in cell numbers on Day 7 compared with those on Day 1 under 1.1% and 2.7% treatment with collagen ($p<0.001$). However, while hBMSCs and hADMSCs also showed increased proliferation under the 2.7% treatment with collagen, the significance was notably lower ($p<0.05$). Specifically, hNTSCs showed a twofold increase in cell number by Day 3 compared to Day 1, surpassing the proliferation of the other hMSCs, as confirmed by the WST-8 assay (Fig. 1c). Cell viability was assessed by incubating cells with a culture medium containing the WST-8 assay reagent and measuring absorbance values. On Day 7, hNTSCs showed values of 0.3 or higher, representing a relatively greater absolute value compared to other hMSCs ($p<0.001$). Live/Dead staining was performed to evaluate the spatial distribution of live and dead cells up to Day 7. We analyzed the viability and proliferation of hNTSCs, hBMSCs, and hADMSCs within 3D-bioprinted constructs. Our evaluation focused on

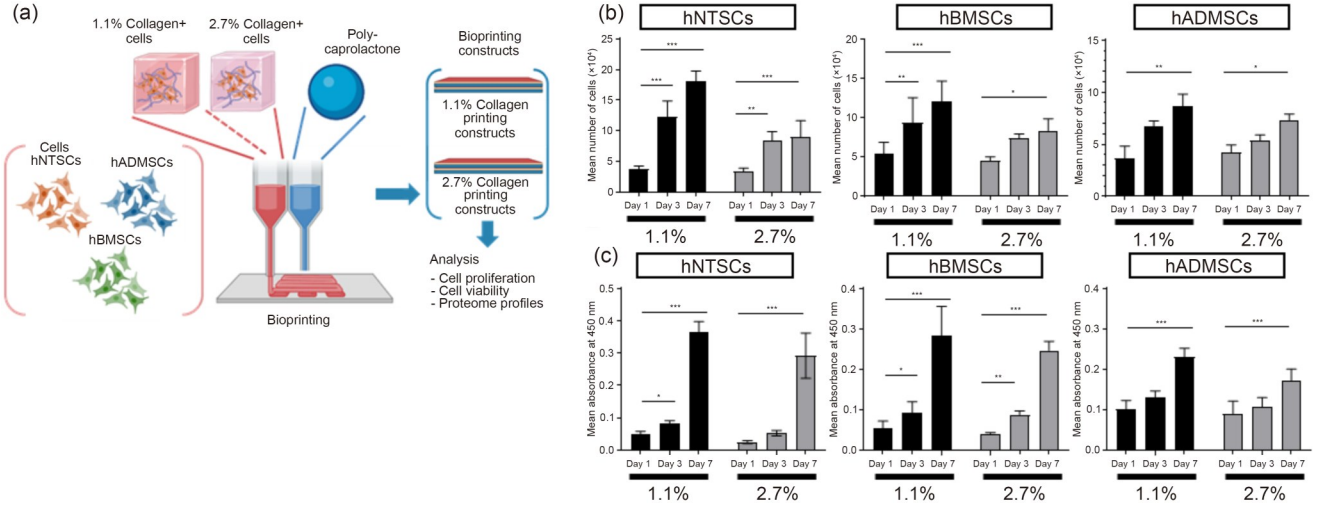

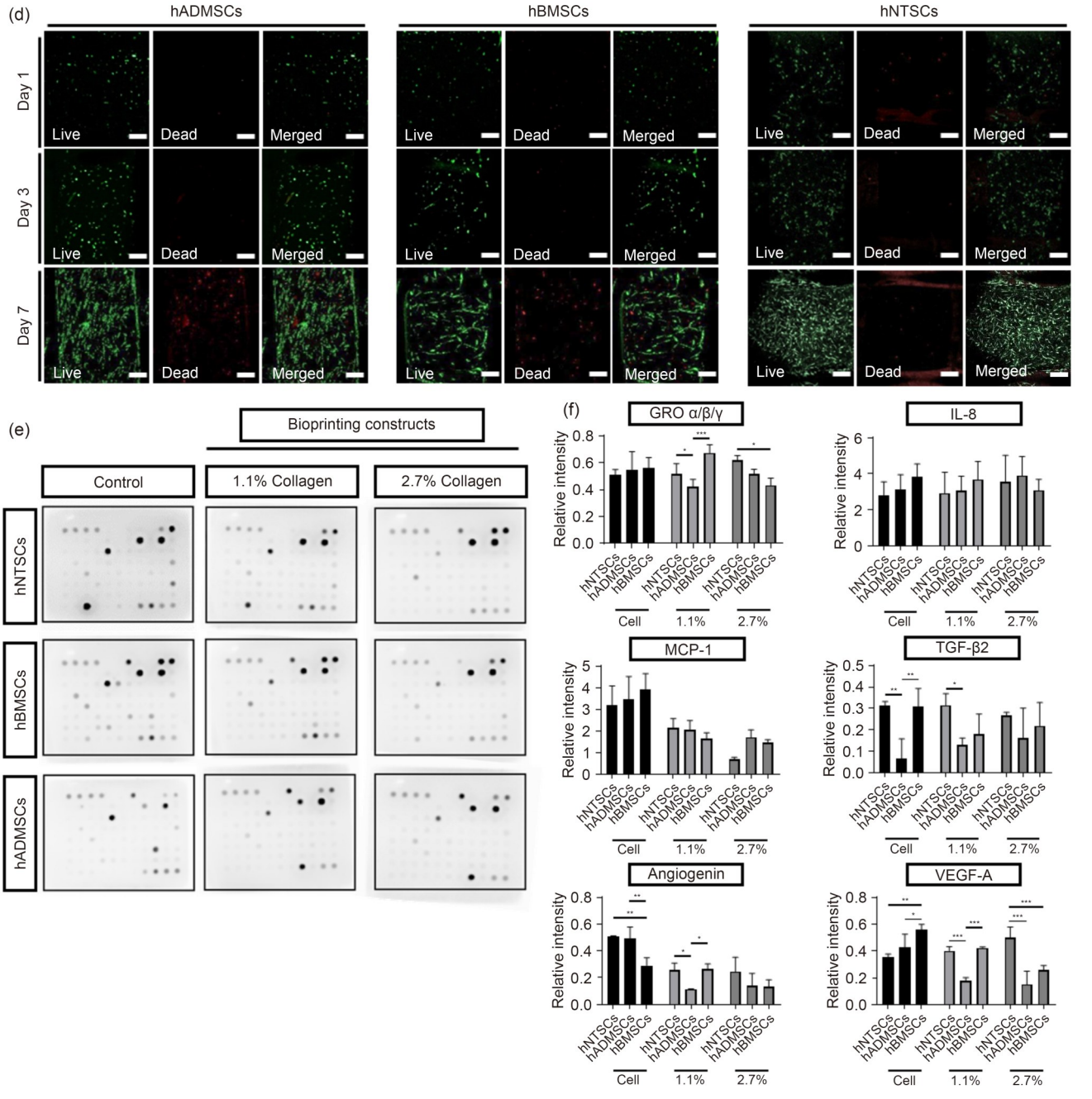

Fig. 1 Comparative analysis of 3D-bioprinted constructs using different stem cell types and collagen concentrations. (a) Schematic overview of 3D-bioprinted construct fabrication using hNTSCs, hBMSCs, and hADMSCs with PCL scaffolds and two collagen concentrations (1.1% and 2.7%). (b) Quantitative analysis of cell proliferation in 3D-bioprinted constructs over 7 d. Total cell counts indicated significant proliferation in all cell types, with hNTSCs showing notably higher proliferation from Day 3 ($^{***}p<0.001$ for hNTSCs; $^{*}p<0.05$ for hBMSCs and hADMSCs, compared with Day 1). Data are presented as mean±SD. (c) WST-8 assay results showing comparative cell growth rates in 3D-bioprinted constructs. hNTSCs exhibited significantly higher proliferation rates by Day 7 (OD>0.3, $^{***}p<0.001$). Data are presented as mean±SEM. (d) Live/Dead cell visualization in the 2.7% treatment with collagen over 7 d using confocal microscopy (Z-stack projections). Green fluorescence indicates live cells, and red fluorescence indicates dead cells. Images show sustained cell viability and proliferation across all cell types. Scale bars: 200 μm. (e) Protein expression analysis using Human Cytokine Array C-5 (80 proteins), comparing secreted factors among different cell types and collagen concentrations (complete protein list: https://www.rndsystems.com/). (f) Quantitative analysis of specific cytokine expression. Data are presented as mean pixel density±SEM (n=5; $^{*}p<0.05$, $^{**}p<0.01$, and $^{***}p<0.001$). Statistical significance was assessed using one-way ANOVA followed by Tukey's post hoc test. OD: optical density

the higher 2.7% collagen concentration for two reasons: first, the denser matrix presents a more stringent environment that typically limits cell proliferation, yet we observed normal cell proliferation under these conditions; second, previous

studies have shown that hMSCs cultured in stiffer 3D environments exhibit increased expression of osteogenic markers. Excessive cell death was not observed, and cell proliferation increased over time (Fig. 1d). To examine how secreted proteins from hMSCs vary according to cell type and collagen concentration, cytokine assays were conducted to evaluate changes in protein secretion in response to varying substrate stiffness (Fig. 1e). Specifically, under 1.1% collagen treatment, growth-regulated oncogene (GRO) α/β/γ secretion was significantly higher in hNTSCs than in hADMSCs ($p<0.05$) and significantly higher in hBMSCs than in hADMSCs ($p<0.001$). Under 2.7% collagen treatment, hBMSCs exhibited the lowest secretion level (Fig. 1f). Transforming growth factor beta 2 (TGF-β2) secretion showed significant differences under cell-only conditions, with both hNTSCs and hBMSCs exhibiting higher secretion than hADMSCs ($p<0.01$). In the 1.1% treatment with collagen, hNTSCs exhibited significantly higher TGF-β2 secretion than hADMSCs (Fig. 1f, $p<0.05$). Angiogenin secretion was significantly higher in both hNTSCs and hADMSCs than in hBMSCs ($p<0.01$) under cell-only conditions. Specifically, in the 1.1% treatment with collagen, hNTSCs and hBMSCs showed significantly higher angiogenin secretion than hADMSCs (Fig. 1f, $p<0.05$). Vascular endothelial growth factor A (VEGF-A) secretion patterns were more complex: under cell-only conditions, hBMSCs secreted more VEGF-A than hNTSCs ($p<0.01$) and hADMSCs ($p<0.05$). However, under 1.1% collagen treatment, VEGF-A secretion was significantly lower in hADMSCs than in both hNTSCs and hBMSCs ($p<0.001$). Under 2.7% collagen treatment, hNTSCs showed significantly higher VEGF-A secretion than hADMSCs and hBMSCs (Fig. 1f, $p<0.001$). Monocyte chemoattractant protein-1 (MCP-1) and interleukin-8 (IL-8) secretions showed no statistically significant differences among cell types across all experimental conditions (Fig. 1f). These results indicate that collagen-based hNTSCs bioprinted constructs with 2.7% collagen possess comparable potential to hBMSCs and hADMSCs, which are commonly used cell sources for 3D bioprinting. Overall, we confirmed that cell survival, proliferation, and secreted protein profiles within the 3D-bioprinted constructs supported their utility for bone regeneration.

3.2 Biomechanical compatibility of the 3D-bioprinted constructs

The mechanical and rheological properties of the 3D-bioprinted constructs were evaluated to assess their physical suitability for implantation and cell encapsulation. Uniaxial compression testing revealed that constructs for both the acute toxicity and tibial defect models exhibited adequate compressive resistance. The elastic modulus (E) was (29.425±1.952) MPa for the acute model and (44.391± 2.828) MPa for the tibial model (n=8 per group), indicating mechanical robustness suitable for bone tissue environments (Table 1).

Table 1 Comparison of compressive modulus (E) between PCL scaffolds and native bone tissues

Sample	E (MPa)
Cortical bone	3000–30,000
Cancellous bone	20–500
PCL scaffold (acute toxicity)	29.425±1.952
PCL scaffold (tibial defect model)	44.391±2.828

Rheological analysis showed that both the 1.1% and 2.7% collagen-based bioinks exhibited typical shear-thinning behavior, with viscosity decreasing as the shear rate increased from 10 to 1000 s^{-1} (Fig. 2). This flow behavior is ideal for extrusion-based bioprinting, ensuring consistent material deposition and preservation of printed structures. Notably, the 2.7% formulation maintained higher viscosity across all shear rates, potentially enhancing post-printing shape fidelity. These physical characterizations confirm that the constructs possess both the mechanical integrity and printability required for stable implantation and biological functionality.

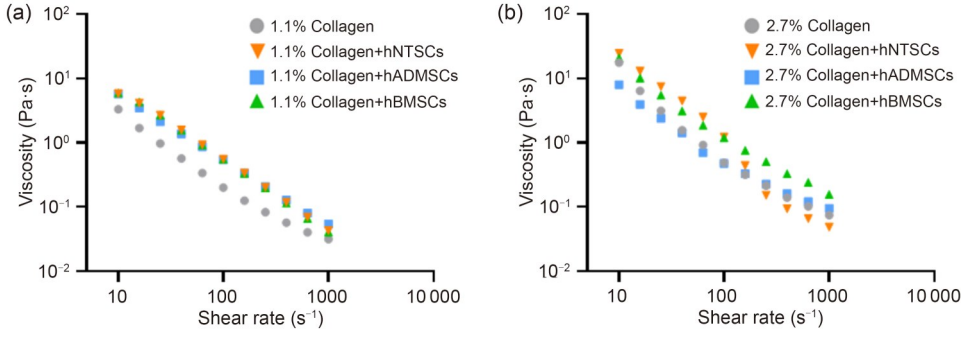

Fig. 2 Shear-thinning behavior of collagen-based bioinks at different concentrations with or without cells. (a) Viscosity profiles of 1.1% collagen-based bioinks with or without cells. (b) Viscosity profiles of 2.7% collagen-based bioinks with or without cells

3.3 3D bioprinting process and somatic mutation analysis

To assess genomic stability during the 3D bioprinting process, somatic mutations and CNVs were analyzed using WGS. Somatic variants and CNVs were selected as key indicators of genomic integrity, as they represent permanent alterations rather than transient changes. Somatic mutations were quantified in constructs containing 1.1% and 2.7% collagen, and total mutation counts were determined for each cell type. The total mutation counts uniquely identified during 3D bioprinting were 1728, 1282, and 1305 for hADMSCs, hBMSCs, and hNTSCs, respectively, in the 1.1% treatment with collagen, and 2786, 1624, and 335 for the 2.7% treatment with collagen (Fig. 3a). Nonsynonymous mutations that could alter protein sequences were also uniquely counted, yielding 5, 6, and 7 for hADMSCs, hBMSCs, and hNTSCs, respectively, in the 1.1% treatment with collagen, and 20, 11, and 2 in the 2.7% treatment with collagen, representing less than 1% of total mutations (Fig. 3b). Using ANNOVAR for annotation, potentially deleterious variants were evaluated based on the nine criteria outlined in Table 2. The unique counts of such variants were 3, 5, and 0 for hADMSCs, hBMSCs, and hNTSCs in the 1.1% treatment with collagen, and 9, 4, and 1 in the 2.7% treatment with collagen, respectively (Fig. 3c). To examine potential disease associations, variant annotations were queried against the ClinVar and COSMIC CGC databases (Tables 3–6). Only a single variant was recorded in ClinVar, which lacked clear disease associations. In the CGC database, which focuses on variants in tumor suppressor genes and/or oncogenes, only two of 78 variants caused protein sequence changes. WGS analysis also identified mutations that occurred in the early bioprinting steps but were absent in subsequent steps. These variants, designated "Mut_Weird," were assessed for allele frequency relative to the other variants. The results showed that the Mut_Weird variants exhibited significantly lower allele frequencies (Fig. 3d), indicating smaller effect sizes. Across all samples, the median allele frequency was 0.16 for Mut_Weird variants versus 0.20 for other variants (p=1.97×10^{-167}). Mut_Weird variants exhibited significantly lower allele frequencies than other variants

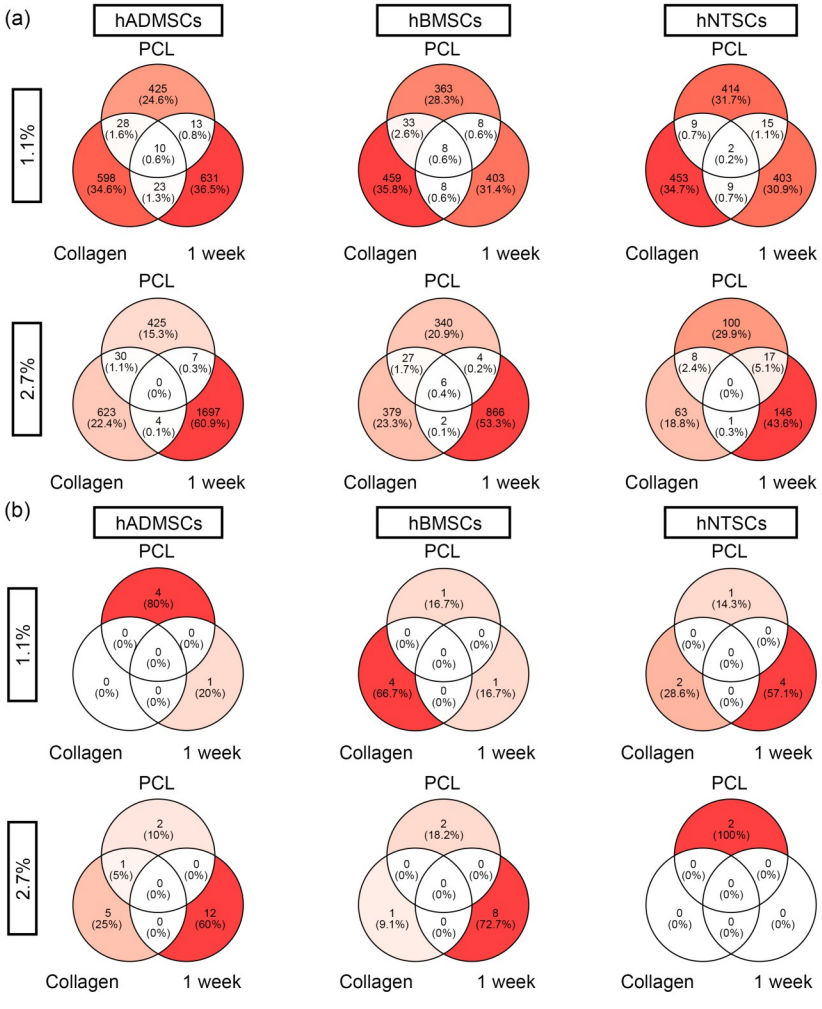

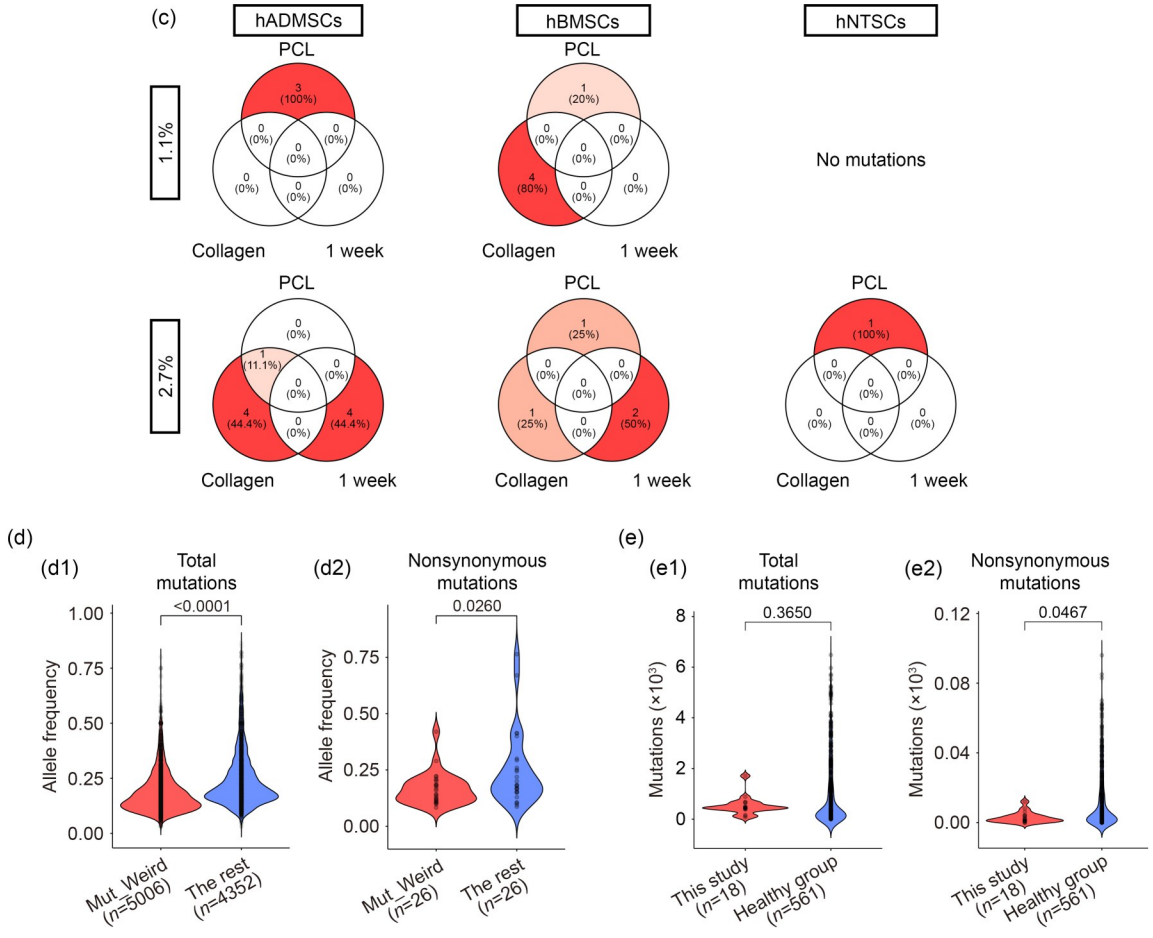

Fig. 3 3D bioprinting process and somatic mutation analysis. (a) Quantitative analysis of total somatic mutations identified during the 3D bioprinting process under 1.1% and 2.7% treatment with collagen: hADMSCs (unique/whole 4458/4639 mutations), hBMSCs (unique/whole 2890/3016 mutations), and hNTSCs (unique/whole 1598/1703 mutations). (b) Analysis of nonsynonymous mutations affecting protein-coding sequences: hADMSCs (unique/whole 25/26 mutations), hBMSCs (unique/whole 17/17 mutations), and hNTSCs (unique/whole 9/9 mutations). These variants represent less than 1% of all mutations, with approximately 10 or fewer mutations identified at each bioprinting stage. (c) Deleterious mutation analysis using ANNOVAR based on nine predefined criteria (Table 2): hADMSCs (unique/whole 16/17 mutations), hBMSCs (unique/whole 11/11 mutations), and hNTSCs (unique/whole 1/1 mutation). Variants were further evaluated for disease associations using the ClinVar and COSMIC CGC databases. (d) Comparative analysis of allele frequency distributions in total mutations and nonsynonymous mutations across three bioprinting stages: collagen culture, PCL scaffold integration, and a 1-week incubation period. "Mut_Weird" represents mutations identified at specific stages but absent in subsequent steps. The analysis showed 5006 Mut_Weird versus 4352 other mutations for total mutations (d1) and 26 mutations each for nonsynonymous variants (d2). (e) Distribution of somatic mutation counts compared with Moore et al. [43]. The reference dataset included 561 nonpathological samples spanning 29 tissue types from 14 donors (labeled "Healthy group (n= 561)" on the x-axis). For (a–c), minor deviations may still occur due to the inherent limitations of rounding

(one-tailed Mann–Whitney U test), suggesting minimal mutational impact during the bioprinting process. For nonsynonymous mutations, the median allele frequencies were 0.151 and 0.182, respectively (p=0.0260). Even variants not designated as Mut_Weird showed relatively low allele frequencies, indicating a low overall mutation rate induced by 3D bioprinting. To assess the safety of 3D bioprinting in relation to naturally occurring mutations in the human body, we used the dataset from Moore et al. [43]. Somatic mutation analysis utilized untreated samples as references; therefore, only data from treated samples were presented, allowing detection of mutations exclusively associated with the bioprinting process. The dataset, based on WGS, examines somatic mutations that gradually accumulate in normal human cells and tissues over a lifetime. Our analysis (Fig. 3e) revealed that mutation counts in 18 3D-bioprinted samples were comparable across all mutations, while nonsynonymous mutations were significantly lower (two-tailed Mann–Whitney U test). These findings indicate mutational stability during 3D bioprinting. In addition to small-scale somatic variations, we assessed somatic CNV gains and losses in 3D-bioprinted samples compared to controls. Across most genomic loci, log2-scaled copy ratios remained close to zero, indicating that 3D bioprinting did not significantly induce

Table 2 Criteria for deleterious mutation analysis using ANNOVAR

Criterion	Categorical prediction
SIFT	D: deleterious (sift≤0.05); T: tolerated (sift>0.05)
SIFT_4G	D: deleterious (sift≤0.05); T: tolerated (sift>0.05)
PolyPhen-2 HDIV	D: probably damaging (pp2_hdiv≥0.957); P: possibly damaging (0.453≤pp2_hdiv<0.957); B: benign (pp2_hdiv<0.453)
PolyPhen-2 HVar	D: probably damaging (pp2_hvar≥0.909); P: possibly damaging (0.447≤pp2_hvar<0.909); B: benign (pp2_hvar<0.447)
LRT	D: deleterious; N: neutral; U: unknown
MutationTaster	A: disease-causing_automatic (harmful); D: disease-causing (harmful); N: polymorphism; P: polymorphism_automatic
MutationAssessor	H: high (harmful); M: medium; L: low; N: neutral; H/M=functional; L/N=nonfunctional
FATHMM	D: deleterious; T: tolerated
PROVEAN	D: deleterious; N: neutral

A list of nine predefined criteria was used to evaluate the potential deleterious effects of variants identified during the 3D bioprinting process in hBMSC, hADMSC, and hNTSC samples. The predicted hazard of mutations was derived from ANNOVAR (https://annovar.openbioinformatics.org/en/latest/user-guide/filter/) and dbSFP (https://brb.nci.nih.gov/seqtools/colexpanno.html#dbnsfp)

Table 3 Number of nonsynonymous mutations

Sample	Missense_ Mutation	Nonsense_ Mutation	Splice_ Site	Frame_ Shift_Del	Frame_ Shift_Ins	In_Frame_ Del	In_Frame_ Ins	Total
sample_Cell_Collagen_1_1_hNTSCs	0	0	1	0	0	1	0	2
sample_Cell_Collagen_1_1_hADMSCs	0	0	0	0	0	0	0	0
sample_Cell_Collagen_1_1_hBMSCs	4	0	0	0	0	0	0	4
sample_Cell_Collagen_2_7_hNTSCs	0	0	0	0	0	0	0	0
sample_Cell_Collagen_2_7_hADMSCs	5	0	0	0	0	0	1	6
sample_Cell_Collagen_2_7_hBMSCs	1	0	0	0	0	0	0	1
sample_Cell_Collagen_PCL_1_1_hNTSCs	1	0	0	0	0	0	0	1
sample_Cell_Collagen_PCL_1_1_hADMSCs	3	1	0	0	0	0	0	4
sample_Cell_Collagen_PCL_1_1_hBMSCs	1	0	0	0	0	0	0	1
sample_Cell_Collagen_PCL_2_7_hNTSCs	1	0	0	0	1	0	0	2
sample_Cell_Collagen_PCL_2_7_hADMSCs	2	0	1	0	0	0	0	3
sample_Cell_Collagen_PCL_2_7_hBMSCs	2	0	0	0	0	0	0	2
sample_Cell_Collagen_PCL_1week_1_1_hNTSCs	0	0	0	0	3	0	1	4
sample_Cell_Collagen_PCL_1week_1_1_hADMSCs	0	0	0	0	0	1	0	1
sample_Cell_Collagen_PCL_1week_1_1_hBMSCs	1	0	0	0	0	0	0	1
sample_Cell_Collagen_PCL_1week_2_7_hNTSCs	0	0	0	0	0	0	0	0
sample_Cell_Collagen_PCL_1week_2_7_hADMSCs	8	0	0	0	3	0	1	12
sample_Cell_Collagen_PCL_1week_2_7_hBMSCs	4	1	1	0	1	1	0	8

CNVs (Fig. 4a). These findings were further supported by CNV visualization in the heatmap (Fig. 4b). In summary, stem cell-based 3D bioprinting maintained genomic stability, a key requirement for ensuring therapeutic safety.

3.4 Acute toxicity analysis of 3D-bioprinted constructs (hematologic parameters and clinical biochemistry parameters)

Toxicity evaluations were conducted under the 2.7% collagen-based bioprinting conditions. Acute toxicity was assessed in constructs bioprinted with hNTSCs, hADMSCs, and hBMSCs. These constructs were subcutaneously implanted into nude mice, followed by hematologic and serum analyses on Days 1, 7, and 14. Pathological examinations were also performed at the implantation site and in five major organs (Fig. 5a). To evaluate acute inflammatory responses and initial biological reactions following implantation across different hMSC-derived constructs, hematologic and serum profiles were analyzed. Results showed a significant increase in the WBC counts in the hBMSCs group ($p<0.05$) and the hADMSCs group ($p<0.01$) compared with controls on Day 1. On Day 7, a significant increase in WBC counts was observed in the 3D-bioprinted construct group without hMSCs (Fig. 5b, $p<0.05$). Various blood biochemical analyses revealed that lactate dehydrogenase in plasma (LDH-P) levels on Day 1 ($p<0.01$) were significantly lower than those of the control group (Fig. 5c). To evaluate the effect of

Table 4 ClinVar and COSMIC CGC database analysis of variants in hMSCs

Sample	ClinVar	CGC (total)	CGC (somatic)	CGC (germline)
sample_Cell_Collagen_1_1_hNTSCs	1	3	3	0
sample_Cell_Collagen_1_1_hADMSCs	0	8	7	1
sample_Cell_Collagen_1_1_hBMSCs	0	6	5	2
sample_Cell_Collagen_2_7_hNTSCs	0	0	0	0
sample_Cell_Collagen_2_7_hADMSCs	0	4	4	1
sample_Cell_Collagen_2_7_hBMSCs	0	2	1	1
sample_Cell_Collagen_PCL_1_1_hNTSCs	0	3	3	1
sample_Cell_Collagen_PCL_1_1_hADMSCs	0	1	1	0
sample_Cell_Collagen_PCL_1_1_hBMSCs	0	3	3	0
sample_Cell_Collagen_PCL_2_7_hNTSCs	0	0	0	0
sample_Cell_Collagen_PCL_2_7_hADMSCs	0	3	3	0
sample_Cell_Collagen_PCL_2_7_hBMSCs	0	5	5	0
sample_Cell_Collagen_PCL_1week_1_1_hNTSCs	0	3	1	2
sample_Cell_Collagen_PCL_1week_1_1_hADMSCs	0	8	7	1
sample_Cell_Collagen_PCL_1week_1_1_hBMSCs	0	1	1	0
sample_Cell_Collagen_PCL_1week_2_7_hNTSCs	0	1	1	1
sample_Cell_Collagen_PCL_1week_2_7_hADMSCs	0	20	20	3
sample_Cell_Collagen_PCL_1week_2_7_hBMSCs	0	7	7	1

Mutation annotation (disease associations): Summary of variant annotations from ClinVar and COSMIC CGC databases for mutations identified in three types of hMSCs during the 3D bioprinting process, including information on disease associations and protein sequence changes. As some mutations in CGC genes can be categorized as both somatic and germline, the total number of CGC mutations in a given sample may not equal the sum of these two categories

Table 5 Variant annotation with the ClinVar database

Hugo symbol	Genome change	Protein change	Sample	Disease	Clinical significance
ATXN1	g.chr6:16327676_16327678delTGA	p.H211del	sample_Cell_Collagen_1_1_451	Not specified	Uncertain significance

Summary of variant annotations from the ClinVar database for mutations identified in hMSCs during the 3D bioprinting process, including disease associations and protein sequence changes

Table 6 Variant annotation with the COSMIC CGC database

Hugo symbol	Genome change	Protein change	Sample	Cancer
ATRX	g.chrX:77508423_77508443del TGGCTGCATACCACCAGCCAC	p.VAGGMQP2463del	sample_Cell_Collagen_PCL_1week_1_1_hADMSCs	Pancreatic neuroendocrine tumors; pediatric GBM
GNAS	g.chr20:58890424A>C	p.I182L	sample_Cell_Collagen_PCL_1week_2_7_hBMSCs	Pituitary adenoma

GBM: glioblastoma. CGC annotation: Only two variants among 78 identified in CGC genes resulted in protein sequence changes. Summary of variant annotations from the COSMIC CGC database for mutations identified in hMSCs during the 3D bioprinting process, including disease associations and protein sequence changes

subcutaneously implanted 3D-bioprinted constructs on BALB/c nude mice, histopathological analyses were conducted under various conditions from Day 1 to Day 14, with examination of the five major organs on Day 14 (Fig. 6). Subcutaneous tissue analysis post-implantation revealed leukocyte infiltration between the 3D-bioprinted constructs and surrounding tissue (Fig. 6a). Inflammatory cell infiltration decreased over time. High-magnification Giemsa staining (Fig. S6 in the supplementary information) revealed only minimal lymphocyte presence in subcutaneous tissue detected across all groups at both Days 1 and 14 post-implantation. All construct types exhibited resolving, low-grade inflammatory responses, with hNTSC constructs showing the least cellular infiltration and hADMSC and hBMSC constructs exhibiting comparable levels of biocompatibility (Fig. 6a).

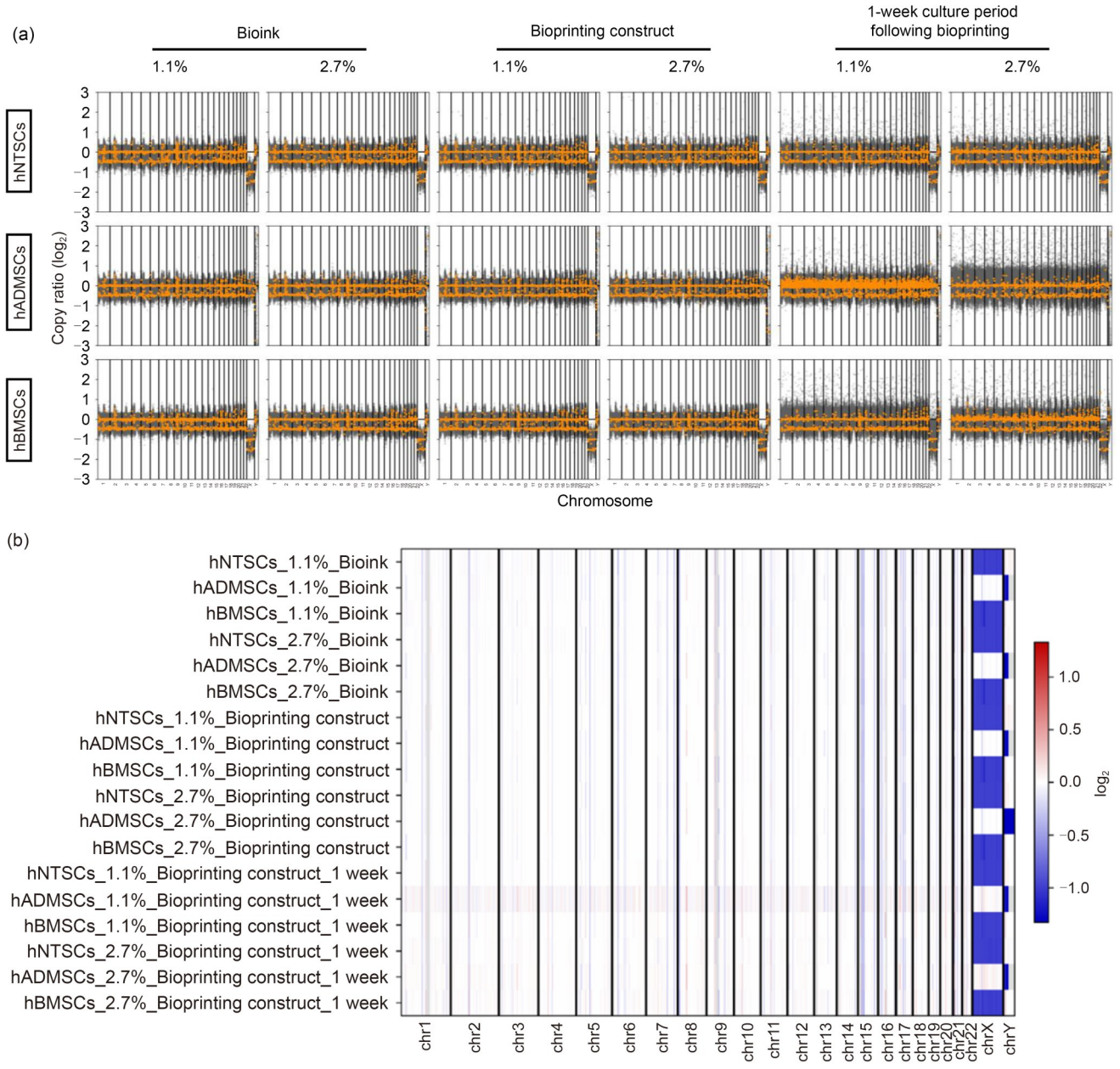

Fig. 4 Analysis of somatic copy number variations during the 3D bioprinting process. (a) Genome-wide analysis of somatic CNV in hADMSCs, hBMSCs, and hNTSCs during the 3D bioprinting process. $\log_2$-scaled copy number ratios were calculated relative to the control samples, with values remaining close to zero across most genomic loci, indicating minimal CNV induction during the process. (b) Heatmap visualization of CNV distributions across chromosomal regions in hADMSCs, hBMSCs, and hNTSCs. Color intensity reflects the magnitude of CNV, supporting overall genomic stability throughout bioprinting

3.5 Efficacy analysis of 3D-bioprinted constructs

To evaluate the therapeutic potential and safety of the 3D-bioprinted constructs, we implanted them in a rabbit bone defect model. Hematologic and serum analyses were performed over a 6-month period to identify potential specific safety concerns, and histological analysis was performed to assess therapeutic outcomes (Fig. 7a). Hematologic results showed a significant increase in hemoglobin (Hb) levels in the hNTSC-bioprinted ($p<0.05$) and hADMSC-bioprinted construct groups ($p<0.01$) compared with controls at week 1 (Fig. 7b). At 6 months, a significant increase in MO levels was observed in the hBMSC-bioprinted construct group (Fig. 7b, $p<0.05$). Blood biochemistry results indicated a significant decrease in LDH-P levels across all hMSCs-containing construct groups at week 1 (Fig. 7c). At 6 months, a significant increase in aspartate aminotransferase

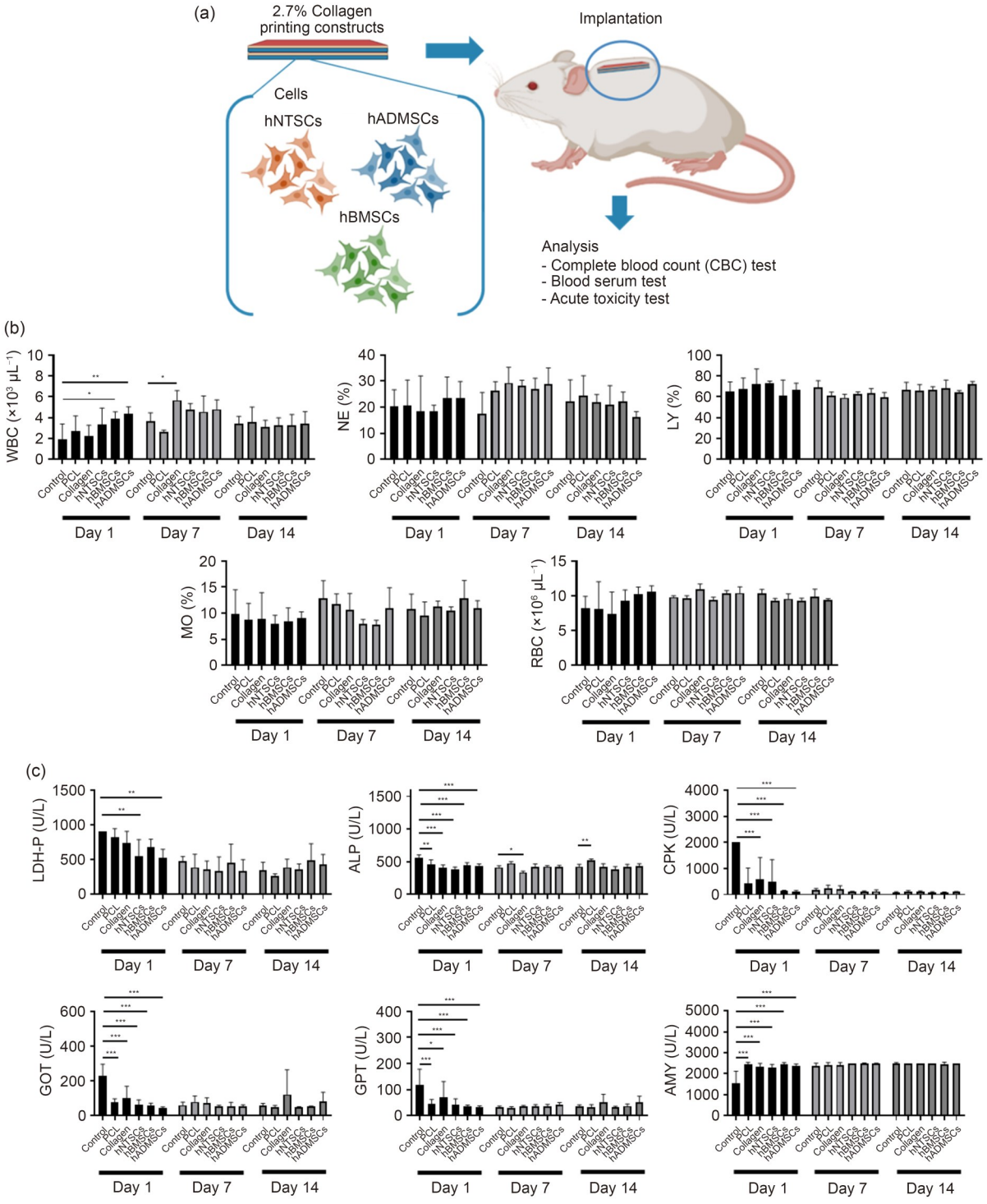

Fig. 5 Acute toxicity assessment of 2.7% collagen-based 3D-bioprinted constructs in nude mice using blood and serum analyses. (a) Schematic overview of the experimental design for acute toxicity evaluation of 3D-bioprinted constructs following subcutaneous implantation in nude mice, including blood testing and organ collection. (b) Quantitative analysis of complete blood count parameters. (c) Analysis of serum biochemical parameters. Data are presented as mean±SEM (n=5; $^{*}p$<0.05, $^{**}p$<0.01, and $^{***}p$<0.001). WBC: white blood cell; NE: neutrophil; LY: lymphocyte; MO: monocyte; RBC: red blood cell; LDH-P: lactate dehydrogenase in plasma; ALP: alkaline phosphatase; CPK: creatine phosphokinase; GOT: glutamic oxaloacetic transaminase (also referred to as AST, aspartate aminotransferase); GPT: glutamic pyruvic transaminase (also referred to as ALT, alanine aminotransferase); AMY: amylase

(AST) levels was observed in the hNTSC- and hBMSC-bioprinted construct groups (Fig. 7c, p<0.05). Therapeutic potential was assessed 6 months post-implantation in a rabbit bone defect model. Histological staining and analysis

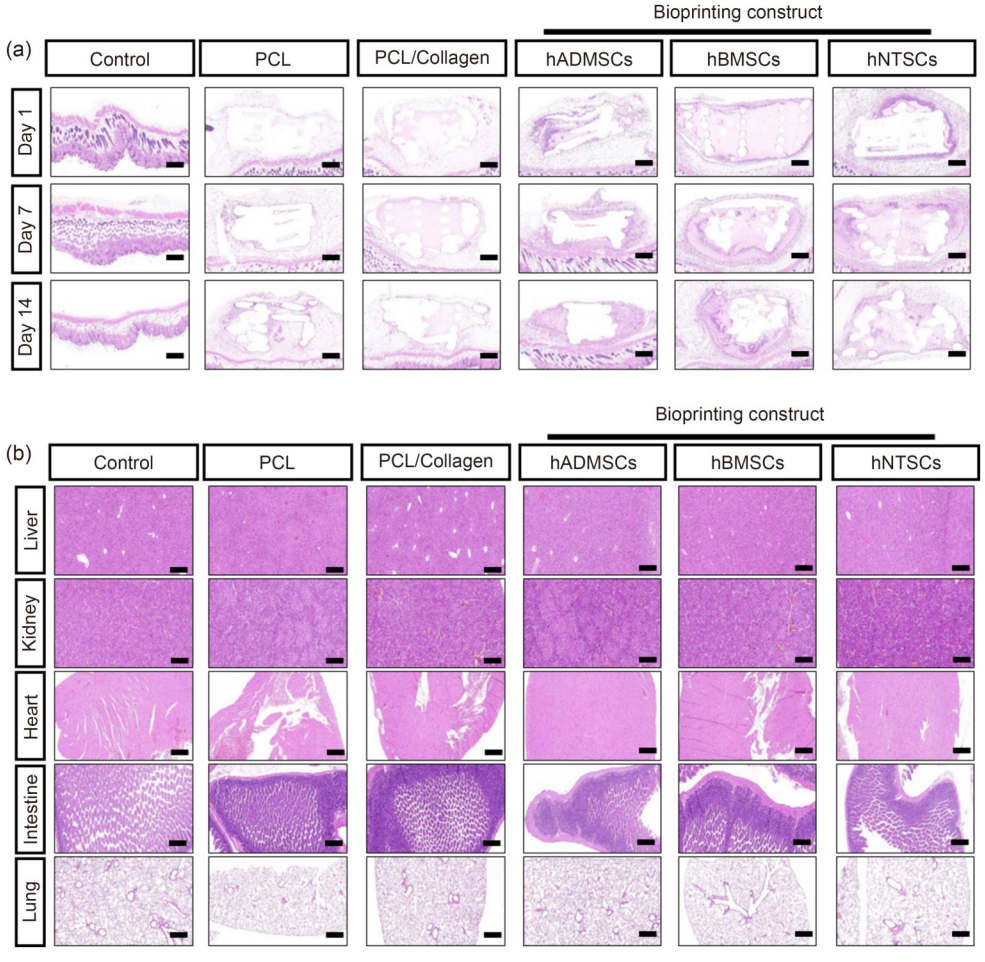

Fig. 6 Histopathological evaluation of 3D-bioprinted constructs and major organs following subcutaneous implantation in nude mice. (a) H&E-stained sections of subcutaneous implantation sites at Days 1, 7, and 14 post-implantation. Initial leukocyte infiltration was observed between the 3D-bioprinted constructs and surrounding tissue, with the presence of inflammatory cells diminishing over time. High-magnification Giemsa staining (Fig. S6 in the supplementary information) confirmed only sparse lymphocytes across all groups. hNTSCs exhibited the lowest degree of cellular infiltration, while hBMSCs and hADMSCs showed comparable low-grade responses. (b) H&E-stained sections of five major organs at Day 14 post-implantation showed no significant pathological changes, indicating a localized and resolving tissue response. Scale bars: 400 μm

revealed persistent defects in the lower region of the implanted structure in the hADMSC-bioprinted construct group (Fig. 8a). The hBMSC-bioprinted construct group showed less collagen deposition at the implantation site compared to the other groups. Conversely, the hNTSC-bioprinted construct group exhibited structurally stable implantation (Fig. 8b). Furthermore, this group showed a higher abundance of OPN- and RUNX2-positive cells, indicating superior bone regeneration potential (Fig. 8c).

4 Discussion

Stem cell-based therapies hold significant promise in regenerative medicine due to the unique regenerative and reparative properties of stem cells [9]. Unlike other adult cell types, stem cells possess a remarkable capacity for tissue regeneration, making them highly valuable for therapeutic applications [44, 45]. Their rapid in vitro proliferation further provides distinct advantages for transplantation [46]. hMSCs can differentiate into target cell types or secrete therapeutic molecules at lesion sites, thereby promoting functional recovery [47]. However, to translate these technologies into clinical practice, comprehensive preclinical research is essential to evaluate efficacy, safety, and potential risks, including tumorigenicity [48].

Among the various hMSCs, hNTSCs offer several advantages over hBMSCs and hADMSCs. hNTSCs can be isolated from nasal turbinate tissue, which is routinely discarded during common surgical procedures, making their collection minimally invasive and less burdensome for patients [49]. Moreover, hNTSCs exhibit robust self-renewal and multipotent differentiation capacities in vitro, highlighting their therapeutic potential [37, 50–53].

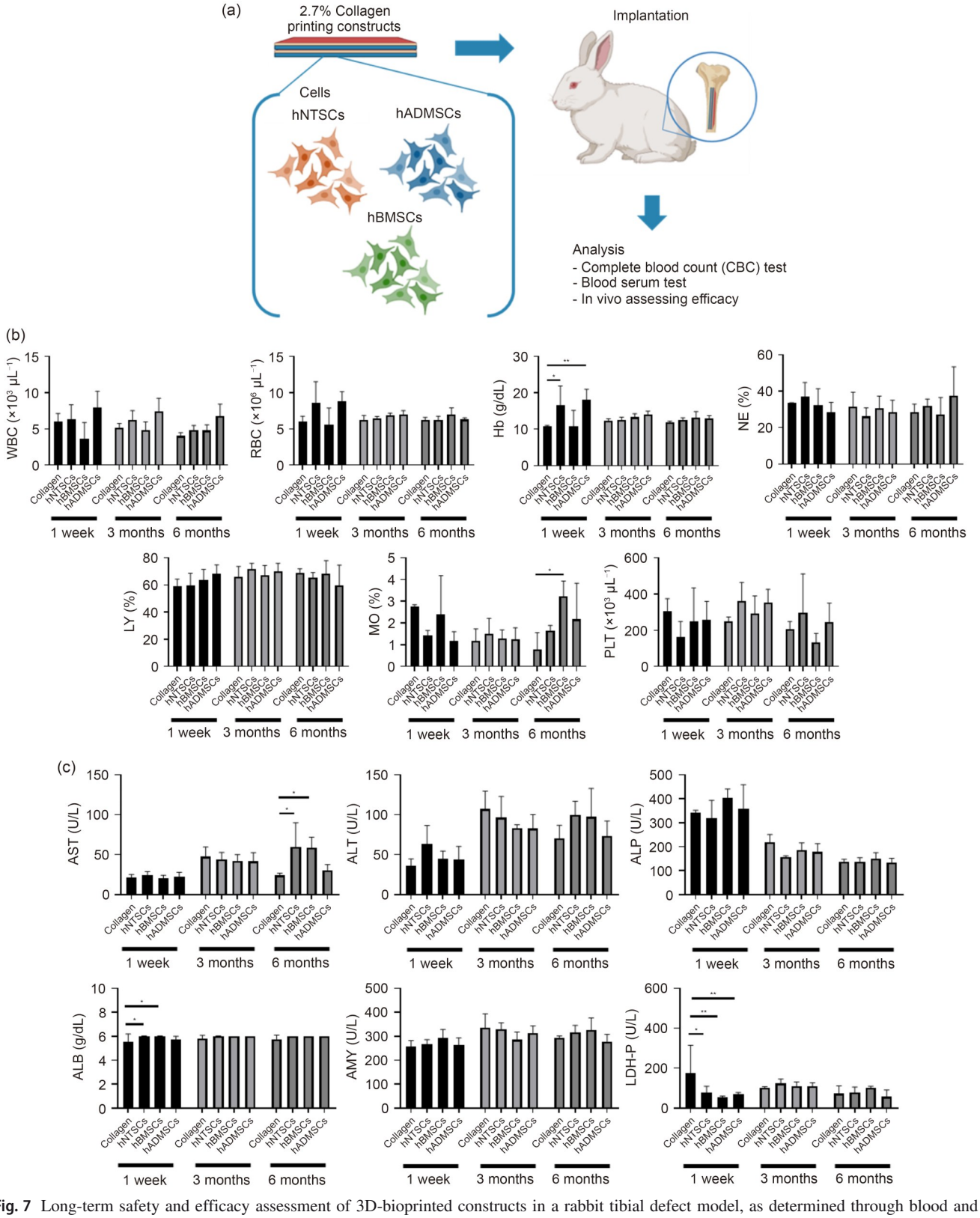

Fig. 7 Long-term safety and efficacy assessment of 3D-bioprinted constructs in a rabbit tibial defect model, as determined through blood and serum analysis. (a) Schematic illustration of the experimental design for evaluating the 2.7% collagen-based bioprinted constructs in rabbit tibial defects over a 6-month period. (b) Temporal analysis of complete blood count parameters. (c) Longitudinal analysis of serum biochemical parameters. Data are presented as mean±SEM (n=5; $^{*}p$<0.05 and $^{**}p$<0.01). WBC: white blood cell; RBC: red blood cell; Hb: hemoglobin; NE: neutrophil; LY: lymphocyte; MO: monocyte; PLT: platelet; AST: aspartate aminotransferase; ALT: alanine aminotransferase; ALP: alkaline phosphatase; ALB: albumin; AMY: amylase; LDH-P: lactate dehydrogenase in plasma

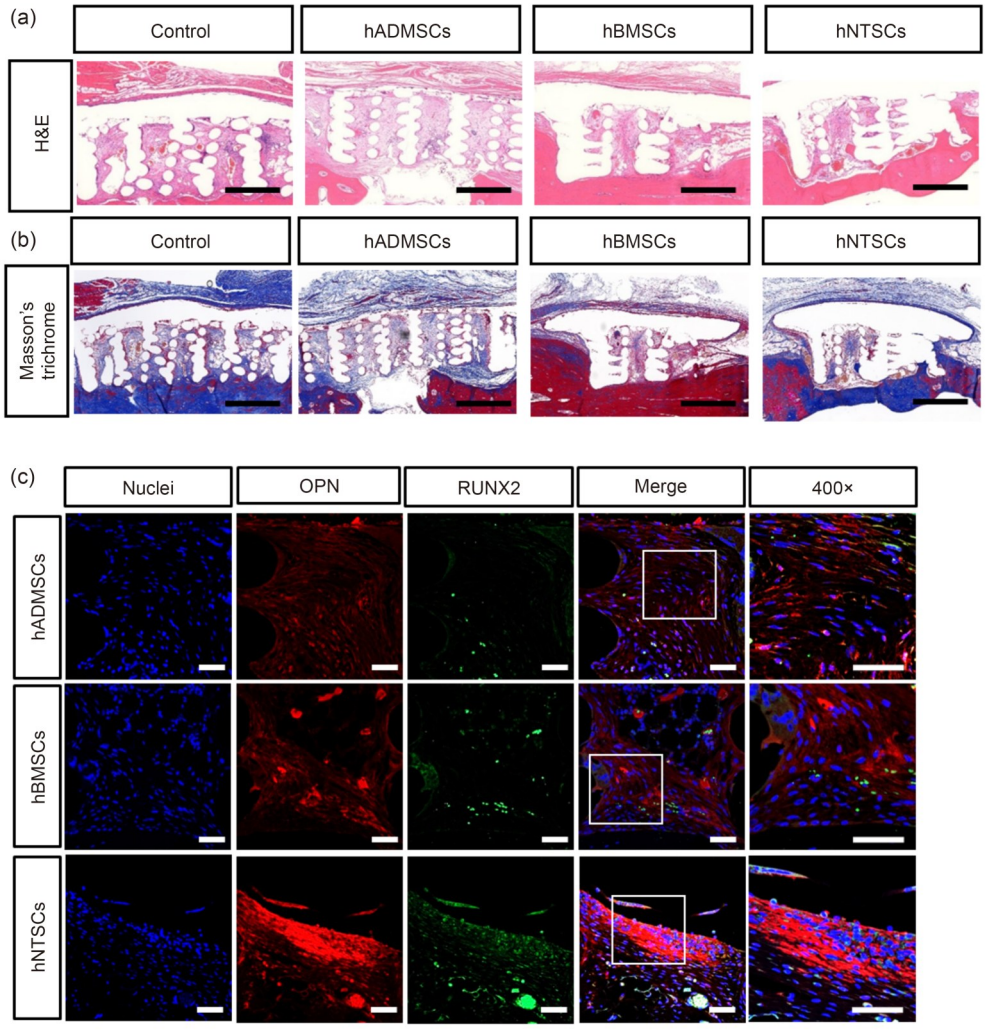

Fig. 8 Histological assessment of bone regeneration following implantation of 3D-bioprinted constructs in rabbit tibial defects. (a) H&E-stained sections of tibial defects at 6 months post-implantation, showing persistent defects in the lower region of the hADMSC construct group. (b) Masson's trichrome staining at 6 months post-implantation, exhibiting reduced collagen distribution in the hBMSC construct group compared with the other groups. The hNTSC construct group showed structurally stable implantation. (c) Immunohistochemical analysis of osteogenic markers (OPN and RUNX2) exhibited enhanced expression in the hNTSC construct group, indicating greater bone regeneration potential. Scale bars: 500 μm

In tissue engineering, 3D bioprinting has emerged as a crucial technology for developing artificial tissues that can replace damaged tissues [54]. This approach incorporates both established and innovative biomaterials to closely replicate the properties of native tissues [55]. For practical clinical applications, these engineered tissues must undergo rigorous preclinical evaluation to confirm both structural stability and safety [56]. Current 3D bioprinting methodologies enable the systematic examination of hMSCs within various scaffold systems, thereby supporting the identification of appropriate materials and cell types for specific lesions [57].

Cell delivery is a crucial determinant of success in stem cell therapies. The integration of stem cells into 3D bioprinting has significantly advanced transplantation techniques by enabling the fabrication of constructs that more closely replicate the native tissue microenvironment [7, 58]. Unlike conventional models, 3D cell and tissue cultures supported by hydrogels allow cells to form tissue-like structures [59]. Hydrogels, commonly referred to as bioinks, protect encapsulated cells from mechanical stress during printing while providing a matrix that supports cell growth and proliferation [60]. Natural biomaterials, such as collagen, gelatin, and fibrin, are commonly used as bioinks in 3D bioprinting due to their structural support and bioactivity properties [61]. In this study, we evaluated the potential of 3D-bioprinted constructs containing hMSCs for bone regeneration. Constructs incorporating hNTSCs, hBMSCs, and hADMSCs were fabricated with PCL and collagen at concentrations of 1.1% and 2.7%. The results indicated that all hMSCs exhibited proliferation within the constructs;

however, hNTSCs exhibited the highest proliferation rates, as confirmed by cell counting and WST-8 assays. Proliferation was higher in the 1.1% collagen concentration than in the 2.7% collagen concentration, with hNTSCs consistently showing superior proliferation rates. Live/Dead cell staining further confirmed minimal cell death across the groups.

hNTSCs also offer distinct advantages in terms of cell procurement due to their minimally invasive collection and strong proliferation capacity. These characteristics suggest that hNTSCs are particularly effective in enhancing the stability of 3D-bioprinted constructs. In tissue engineering, maintaining the viability and proliferation of encapsulated cells remains a vital factor for successful outcomes [62]. Collagen is a safe and effective biomaterial that supports cell proliferation while minimizing cell death [63]. Its widespread application underscores the clinical relevance of 3D bioprinting.

Cytokine assays further revealed that hNTSCs secreted higher levels of VEGF-A, a key factor in angiogenesis, under both collagen conditions. VEGF-A facilitates vascular formation, promotes the differentiation of MSCs into osteogenic cells, increases blood vessel density at the healing site, and enhances bone formation [64]. Although excessive VEGF-A can lead to aberrant vessel formation, the elevated expression observed in hNTSCs suggests a superior potential for bone regeneration [65]. Overall, these findings highlight that hNTSCs possess a greater bone regenerative capacity compared to other hMSCs. Their high VEGF-A secretion, combined with ease of collection, makes them promising candidates for future clinical applications in treating bone loss and defects [66].

Rheological analysis confirmed that the collagen bioinks exhibited shear-thinning behavior, characterized by a decrease in viscosity with increasing shear rate. This property facilitates stable extrusion during bioprinting and maintains high-fidelity shape retention post-printing. Moreover, shear-thinning reduces mechanical stress on encapsulated cells during extrusion, thereby preserving cell viability and promoting homogeneous distribution within the printed matrix [67]. Collectively, these findings indicate that the bioprinted constructs not only offer a supportive cellular microenvironment but also meet the essential mechanical and rheological criteria required for successful integration in cancellous bone tissue engineering.

Beyond cellular performance, the mechanical and rheological characteristics of the constructs further show their applicability in bone tissue engineering. Compression testing showed that the elastic modulus (E) of the bioprinted constructs (29.4–44.3 MPa) fell within the reported range of native cancellous bone (20–500 MPa), indicating sufficient structural integrity for implantation in bone defects. Although cortical bone typically exhibits much higher stiffness (in the GPa range), the measured elastic modulus (E) aligns with cancellous bone properties, supporting its potential use in bone defect repair where moderate mechanical support is adequate [68–70]. Rheological analysis also confirmed shear-thinning behavior, which facilitates stable extrusion during bioprinting, preserves cell viability, and promotes homogeneous distribution within the printed matrix [67]. Collectively, these findings indicate that bioprinted constructs not only create a conducive cellular microenvironment but also satisfy critical mechanical and rheological requirements for successful application in cancellous bone tissue engineering.

DNA sequencing is the most reliable method for detecting somatic mutations, including silent and nontranscribed variants that cannot be identified by RNA-seq [71–73]. Although the bioprinting process is relatively short, the occurrence of rare mutations cannot be wholly excluded, particularly due to the mechanical and thermal stresses applied during printing. Such mutations, even if infrequent, could potentially disrupt oncogenic pathways and pose long-term safety concerns. WGS provides unbiased genome-wide coverage to identify such events and supports compliance with international safety guidelines for cell-based products. Our analysis exhibited negligible genomic instability across all stages of the 3D bioprinting process, reinforcing the safety of this approach for regenerative applications. WGS was performed on samples collected during the 3D bioprinting process to assess genetic stability and identify somatic mutations. The proportion of nonsynonymous mutations in the samples was less than 1% of the total mutations, with most samples containing 10 or fewer variants. Furthermore, the frequency of deleterious mutation types, such as frameshift and nonsense variants, was found to be nearly negligible. To assess the pre-existing and potential harmfulness of the identified mutations, we annotated them using the ClinVar and CGC databases as well as the ANNOVAR tool. The results indicated that harmful variants were rarely detected. WGS further revealed mutations that occurred during the 3D bioprinting process but were absent in the subsequent stages; these were termed “Mut_Weird” in our study. The allele frequencies of these mutations were lower than those of other variants, indicating that their effect size was minimal due to their low allele frequencies. The other mutations also did not have high allele frequencies. CNV analysis was also performed to determine whether 3D bioprinting induced large-scale genomic gains or losses. Although minor variations could not be excluded, no significant genomic instability was observed. Overall, the mutation and CNV rates during 3D bioprinting were relatively low. Notably, hNTSCs exhibited a significantly lower mutation generation rate than hADMSCs and hBMSCs, suggesting that hNTSCs may be more suitable for 3D bioprinting than other hMSCs.

We previously evaluated regenerative outcomes using nude mice, which, despite their immunodeficiency, remain

a valuable model for assessing the direct osteogenic potential of transplanted MSCs. Multiple studies have shown that hBMSCs can form ectopic bone in vivo, and that MSC transplantation enhances bone regeneration and defect repair [74–76]. In our in vitro experiments, hNTSCs exhibited stronger osteogenic differentiation than hBMSCs when cultured in 3D-bioprinted constructs with osteogenic induction medium, as indicated by elevated expression of RUNX2. These findings were consistent with our in vivo results, where constructs containing osteogenically induced hNTSCs promoted greater bone formation in nude mice. Together, these findings suggest that the regenerative effects observed in this model are primarily attributable to the intrinsic osteogenic capacity of MSCs, independent of immune modulation.

Importantly, our previous studies showed that hNTSCs possess potent immunomodulatory properties that remain effective even in compromised immune environments. Lim et al. [39] reported that hNTSCs significantly modulated immune responses by reducing microglia numbers and suppressing the expression of the inflammatory cytokine IL-6 in Alzheimer's disease models. This immunosuppressive capacity was mediated through both direct cell-to-cell contact and paracrine signaling, highlighting the versatility of hNTSCs in immune regulation.

Furthermore, the effectiveness of hNTSCs observed in our immunocompetent rabbit model (Fig. 7) validated the translational relevance of the findings obtained in nude mice. In the rabbit tibial defect model, which possesses a fully functional immune system, constructs containing hNTSCs promoted superior bone regeneration. These outcomes support the dual role of hNTSCs, combining intrinsic osteogenic potential with robust immunomodulatory effects that act synergistically in vivo.

We also evaluated the acute toxicity of 3D-bioprinted constructs using a subcutaneous implantation model in nude mice, specifically examining constructs with 2.7% collagen concentration. An initial inflammatory response was observed, characterized by elevated WBC counts in the hBMSCs and hADMSCs groups. By Day 7, WBC levels had returned to baseline, indicating that the acute inflammatory response was transient.

Histopathological examination of major organs revealed no significant pathological changes. In the subcutaneous tissue, a mild localized inflammatory response was observed following transplantation, which remained stable or slightly decreased between Days 1 and 14. High-magnification Giemsa staining (Fig. S6 in the supplementary information) showed only sparse lymphocytic infiltration, with no evidence of severe cytotoxicity. All construct groups exhibited acceptable biocompatibility, with the hNTSCs group showing the lowest level of inflammatory cell infiltration.

Tissue-engineered scaffolds act as artificial extracellular matrices (ECMs), providing crucial physical and biological support for tissue repair and regeneration [77]. The success of tissue repair depends largely on effective ECM remodeling, which is strongly influenced by the host response to implanted scaffolds [78]. A major challenge is regulating the host inflammatory response, as it plays a decisive role in determining the outcome of ECM remodeling and tissue repair [79–81].

Macrophages play a central role in this process, and their functional plasticity influences the quality of ECM remodeling [82]. Achieving an appropriate balance between pro-inflammatory M1 and anti-inflammatory M2 macrophage phenotypes is crucial for optimal tissue regeneration [83]. While promoting the transition from M1 to M2 macrophages is a key strategy, improper timing or excessive suppression can result in complications, such as delayed wound healing, aberrant ECM deposition, and fibrosis [84, 85].

Xenotransplantation of hMSCs in rabbit models is widely used for preclinical evaluation in regenerative medicine. However, substantial interspecies differences—particularly in immunology, physiology, and cellular biology—can significantly affect the interpretation of results. In this study, we expanded the discussion to address how these differences may have affected the validity and translational relevance of our findings. hMSCs and rabbit MSCs show distinct surface marker expression profiles. hMSCs are typically positive for CD29, CD73, CD90, and CD105, whereas rabbit MSCs exhibit markedly lower expression of CD73 and CD105 and are negative for CD90 [86–88]. For instance, CD90 is expressed in more than 95% of hMSCs but is absent in rabbit MSCs, underscoring the need for species-specific criteria in phenotypic and functional assessments. In our study, MSCs were isolated from the inferior turbinate tissues of 10 human patients undergoing nasal surgery. These hNTSCs exhibited the expected marker profile, being positive for CD29, CD73, and CD90, and negative for CD14, CD19, CD34, and HLA-DR. Their multipotency was confirmed by their ability to differentiate into chondrocytes, osteoblasts, adipocytes, and neuron-like cells, as revealed by immunohistochemistry, reverse transcriptase–polymerase chain reaction (RT-PCR), and Western blotting. These findings highlight the biological relevance and therapeutic potential of hNTSCs for regenerative medicine applications in xenogeneic models [20]. Reports on the survival of hMSCs in rabbit models have been inconsistent. Some studies have documented the presence of viable human cells persisting for up to 12 weeks without immunosuppression [89], whereas others have reported limited survival beyond 10 weeks [90]. These discrepancies are likely attributable to differences in implantation site, MSC source, and host immune response. Although MSCs exhibit immunoprivileged properties, xenogeneic immune responses to species-specific antigens can compromise their long-term viability and functionality [91]. Furthermore, physiological

differences between rabbits and humans—such as bone remodeling rates, immune cell composition, and cytokine receptor compatibility—may restrict the clinical translatability of xenotransplantation findings. Both acute and chronic reactions must be considered, as humoral and cellular immune responses to human antigens can emerge after several weeks, necessitating long-term immune monitoring [92]. Notably, the therapeutic effects of hMSCs in xenogeneic models often arise not from direct differentiation but from paracrine activity. MSCs secrete various growth factors and cytokines—such as VEGF, TGF-β, and insulin-like growth factor-1 (IGF-1)—that promote angiogenesis and tissue regeneration [93]. These observations suggest that the sustained secretion of regenerative factors, rather than cell engraftment alone, is a primary contributor to therapeutic efficacy in xenogeneic settings. In conclusion, while the rabbit model offers valuable preclinical insights, interspecies immunological and biological differences must be carefully considered when interpreting results.

Building on these considerations, we employed hNTSCs in 3D-bioprinted constructs to evaluate their regenerative potential in a rabbit critical-sized bone defect model. hNTSCs represent a novel source of multipotent MSCs with robust osteogenic, chondrogenic, and adipogenic differentiation capacities. Their phenotypic characterization confirmed the expression of typical MSC markers, including CD29, CD73, and CD90, while lacking hematopoietic markers.

Our findings indicate that 3D-bioprinted constructs incorporating hNTSCs are generally biocompatible; however, localized tissue responses were observed, highlighting the need for further study. Therefore, long-term studies are necessary to comprehensively evaluate the biocompatibility, immunogenicity, and functional integration of these constructs before clinical application.

The efficacy of the 3D-bioprinted constructs was evaluated in a rabbit bone defect model over a 6-month period. The results indicated that constructs containing hNTSCs exhibited greater bone regeneration potential than those containing hBMSCs or hADMSCs. This was evidenced by the elevated expression of OPN and RUNX2, both of which are critical markers of bone formation.

OPN, a protein belonging to the small integrin-binding ligand N-linked glycoprotein (SIBLING) family, is involved in various biological processes, particularly bone metabolism and homeostasis [94, 95]. It plays a crucial role in neuron-mediated and endocrine regulation of bone mass and modulates the proliferation, migration, and adhesion of several bone-related cell types, including bone marrow MSCs, hematopoietic stem cells, osteoclasts, and osteoblasts [96]. Its involvement in bone-related diseases, such as osteoporosis, rheumatoid arthritis, and osteosarcoma, further underscores its biological significance [97].

RUNX2 is a key transcription factor essential for skeletal development and is expressed in multipotent mesenchymal cells, osteoblast-lineage cells, and chondrocytes [98]. The Runx2 protein is critical for chondrocyte maturation and osteoblast differentiation, and it regulates osteoprogenitor proliferation and differentiation into preosteoblasts through multiple signaling pathways, including Hedgehog, fibroblast growth factor (FGF), Wnt, and parathyroid hormone-like hormone (PTHLH) [99]. The cotranscription factor Cbfb enhances Runx2 function by stabilizing the protein and preventing ubiquitination, thereby regulating the proliferation and differentiation of chondrocytes and osteoblast-lineage cells [100]. The importance of RUNX2 in bone development is further highlighted by its role in the pathogenesis of conditions such as cleidocranial dysplasia, which is caused by mutations in the *RUNX2* gene [101].

Hematologic and serum analyses conducted over the study period revealed no significant long-term toxicity in any of the construct groups. Notably, constructs containing hNTSCs showed stable structural integration into the bone defect site, whereas constructs with hBMSCs exhibited less collagen distribution, and those with hADMSCs left the defects unresolved.

These findings suggest that hNTSCs are particularly well suited for bone regeneration, with the potential to provide more effective and stable therapeutic outcomes in clinical applications.

5 Conclusions

This study revealed the potential of 3D-bioprinted constructs incorporating hMSCs for bone regeneration. Constructs containing hNTSCs, hBMSCs, and hADMSCs were comprehensively evaluated in combination with PCL and collagen. The results confirmed that these constructs were safe, showed no evidence of tumorigenicity or acute toxicity, and effectively supported cell proliferation and bone regeneration, with hNTSCs exhibiting the strongest regenerative capacity. These findings underscore the importance of extensive preclinical evaluations, including safety assessments with proteomics, next-generation sequencing, and animal models. The superior bone regeneration potential of hNTSCs suggests that this cell type may be particularly suitable for clinical applications in bone tissue engineering. Nonetheless, further research is needed to assess the long-term safety and efficacy of this approach, as well as to optimize the combination of bioprinting materials and cell sources. Addressing these challenges will be essential for the successful translation of 3D bioprinting technologies. Overall, this study provides a solid foundation for future research and clinical trials aimed at developing advanced therapies that leverage the regenerative capacity of MSCs through innovative 3D bioprinting techniques.

Supplementary Information The online version contains supplementary material available at https://doi.org/10.1631/bdm.2500128.

Acknowledgements This research was supported by a grant (No. RS-2024-00397128) from the Ministry of Food and Drug Safety in 2024 and supported by the National Research Foundation of Korea (NRF) grant funded by the Ministry of Science and ICT (No. 2021M3F7A1083232). Furthermore, this work was supported by the National Research Foundation of Korea (NRF) grant funded by the Korean government (MSIT) (Nos. RS-2023-00215891 and 2022R1A2C2008149).

Author contributions JHJ: writing—original draft, validation, methodology, and data curation. JSK, HJJ, ECK, HJY, HWK, and EH: validation and methodology. MSK and JYL: methodology and writing—review and editing. ML, SJL, and SWK: funding acquisition, supervision, project administration, and writing—review and editing.

Declarations

Conflict of interest The authors declare that they have no conflict of interest.

Ethical approval The study procedure using hNTSCs was conducted in compliance with the Institutional Review Board of Seoul St. Mary's Hospital (approval number: KC08TISS0341), The Catholic University of Korea. Written informed consent (both for participation and publication) was obtained from patients before surgery. All mouse research procedures were performed in accordance with the Laboratory Animals Welfare Act, the Guide for the Care and Use of Laboratory Animals, and the Guidelines and Policies for Rodent Experiments provided by the Institutional Animal Care and Use Committee (IACUC) of the College of Medicine, The Catholic University of Korea (approval number: CUMS-2023-0175-02). All rabbit research procedures were performed in accordance with the Laboratory Animals Welfare Act, the Guide for the Care and Use of Laboratory Animals, and the Guidelines and Policies for Experiments provided by the IACUC of the College of Medicine, The Catholic University of Korea (approval number: CUMS-2021-0015-02). The IACUC and Department of Laboratory Animal (DOLA) at The Catholic University of Korea, Songeui Campus, accredited the Korea Excellence Animal Laboratory Facility by the Korea Food and Drug Administration in 2017 and reaccredited it in 2021 and 2025. It also obtained full Association for Assessment and Accreditation of Laboratory Animal Care (AAALAC) International accreditation in 2018 and was reaccredited in 2022 and 2025.

Data availability The datasets used and analyzed during the current study are available from the corresponding authors upon reasonable request.

Use of generative AI tools No generative AI tools were used in the preparation of this manuscript.

References

1. Gurtner GC, Callaghan MJ, Longaker MT (2007) Progress and potential for regenerative medicine. *Annu Rev Med* 58:299–312. https://doi.org/10.1146/annurev.med.58.082405.095329
2. Jankovic MG, Stojkovic M, Bojic S et al (2023) Scaling up human mesenchymal stem cell manufacturing using bioreactors for clinical uses. *Curr Res Transl Med* 71(2):103393. https://doi.org/10.1016/j.retram.2023.103393
3. The Committee for Advanced Therapies (2010) Challenges with advanced therapy medicinal products and how to meet them. *Nat Rev Drug Discov* 9(3):195–201. https://doi.org/10.1038/nrd3052
4. Goula A, Gkioka V, Michalopoulos E et al (2020) Advanced therapy medicinal products challenges and perspectives in regenerative medicine. *J Clin Med Res* 12(12):780–786. https://doi.org/10.14740/jocmr3964
5. Gomes KLG, da Silva RE, da Silva JB et al (2023) Post-marketing authorisation safety and efficacy surveillance of advanced therapy medicinal products in Brazil, the European Union, the United States and Japan. *Cytotherapy* 25(10): 1113–1123. https://doi.org/10.1016/j.jcyt.2023.06.005
6. Han F, Wang J, Ding L et al (2020) Tissue engineering and regenerative medicine: achievements, future, and sustainability in Asia. *Front Bioeng Biotechnol* 8:83. https://doi.org/10.3389/fbioe.2020.00083
7. Tasnim N, De la Vega L, Kumar SA et al (2018) 3D bioprinting stem cell derived tissues. *Cel Mol Bioeng* 11(4):219–240. https://doi.org/10.1007/s12195-018-0530-2
8. Hunsberger JG, Shupe T, Atala A (2018) An industry-driven roadmap for manufacturing in regenerative medicine. *Stem Cells Transl Med* 7(8):564–568. https://doi.org/10.1002/sctm.18-0060
9. Hoang DM, Pham PT, Bach TQ et al (2022) Stem cell-based therapy for human diseases. *Signal Transduct Target Ther* 7(1): 272. https://doi.org/10.1038/s41392-022-01134-4
10. El-Kadiry AE, Rafei M, Shammaa R (2021) Cell therapy: types, regulation, and clinical benefits. *Front Med* 8:756029. https://doi.org/10.3389/fmed.2021.756029
11. Lo B, Parham L (2009) Ethical issues in stem cell research. *Endocr Rev* 30(3):204–213. https://doi.org/10.1210/er.2008-0031
12. Pirsadeghi A, Namakkoobi N, Behzadi MS et al (2024) Therapeutic approaches of cell therapy based on stem cells and terminally differentiated cells: potential and effectiveness. *Cells Dev* 177:203904. https://doi.org/10.1016/j.cdev.2024.203904
13. Olson JL, Atala A, Yoo JJ (2011) Tissue engineering: current strategies and future directions. *Chonnam Med J* 47(1):1–13. https://doi.org/10.4068/cmj.2011.47.1.1
14. Sousa I, Mendes A, Pereira RF et al (2014) Collagen surface modified poly(ε-caprolactone) scaffolds with improved hydrophilicity and cell adhesion properties. *Mater Lett* 134:263–267. https://doi.org/10.1016/j.matlet.2014.06.132
15. Saini G, Segaran N, Mayer JL et al (2021) Applications of 3D bioprinting in tissue engineering and regenerative medicine. *J Clin Med* 10(21):4966. https://doi.org/10.3390/jcm10214966
16. Hu SQ, Ogle BM, Cheng K (2018) Body builder: from synthetic cells to engineered tissues. *Curr Opin Cell Biol* 54:37–42. https://doi.org/10.1016/j.ceb.2018.04.010
17. de Jongh D, Massey EK, Cronin AJ et al (2022) Early-phase clinical trials of bio-artificial organ technology: a systematic review of ethical issues. *Transpl Int* 35:10751. https://doi.org/10.3389/ti.2022.10751
18. Sekar MP, Budharaju H, Zennifer A et al (2021) Current standards and ethical landscape of engineered tissues—3D bioprinting perspective. *J Tissue Eng* 6:1–33. https://doi.org/10.1177/20417314211027677
19. Derks LLM, van Boxtel R (2023) Stem cell mutations, associated cancer risk, and consequences for regenerative medicine. *Cell Stem Cell* 30(11):1421–1433. https://doi.org/10.1016/j.stem.2023.09.008

20. Hwang SH, Kim SY, Park SH et al (2012) Human inferior turbinate: an alternative tissue source of multipotent mesenchymal stromal cells. *Otolaryngol Head Neck Surg* 147(3):568–574. https://doi.org/10.1177/0194599812447172
21. Hwang SH, Park SH, Choi J et al (2013) Age-related characteristics of multipotent human nasal inferior turbinate-derived mesenchymal stem cells. *PLoS ONE* 8(9):e74330. https://doi.org/10.1371/journal.pone.0074330
22. Hwang SH, Park SH, Choi J et al (2014) Characteristics of mesenchymal stem cells originating from the bilateral inferior turbinate in humans with nasal septal deviation. *PLoS ONE* 9(6): e100219. https://doi.org/10.1371/journal.pone.0100219
23. Ewels P, Magnusson M, Lundin S et al (2016) MultiQC: summarize analysis results for multiple tools and samples in a single report. *Bioinformatics* 32(19):3047–3048. https://doi.org/10.1093/bioinformatics/btw354
24. Bolger AM, Lohse M, Usadel B (2014) Trimmomatic: a flexible trimmer for Illumina sequence data. *Bioinformatics* 30(15): 2114–2120. https://doi.org/10.1093/bioinformatics/btu170
25. Li H (2013) Aligning sequence reads, clone sequences and assembly contigs with BWA-MEM. https://arxiv.org/pdf/1303.3997
26. McKenna A, Hanna M, Banks E et al (2010) The Genome Analysis Toolkit: a MapReduce framework for analyzing next-generation DNA sequencing data. *Genome Res* 20(9): 1297–1303. https://doi.org/10.1101/gr.107524.110
27. Benjamin D, Sato T, Cibulskis K et al (2019) Calling somatic SNVs and indels with Mutect2. https://www.biorxiv.org/content/10.1101/861054v1
28. Danecek P, Bonfield JK, Liddle J et al (2021) Twelve years of SAMtools and BCFtools. *Gigascience* 10(2):giab008. https://doi.org/10.1093/gigascience/giab008
29. Wang K, Li MY, Hakonarson H (2010) ANNOVAR: functional annotation of genetic variants from high-throughput sequencing data. *Nucleic Acids Res* 38(16):e164. https://doi.org/10.1093/nar/gkq603
30. Mayakonda A, Lin DC, Assenov Y et al (2018) Maftools: efficient and comprehensive analysis of somatic variants in cancer. *Genome Res* 28(11):1747–1756. https://doi.org/10.1101/gr.239244.118
31. Gómez-Rubio V (2017) Ggplot2-elegant graphics for data analysis (2nd Edition). *J Stat Softw* 77(2):1–3. https://doi.org/10.18637/jss.v077.b02
32. Kassambara A (2018) Ggpubr: 'ggplot2' based publication ready plots. R package version 2. https://CRAN.R-project.org/package=ggpubr [Accessed on 28 November 2023]
33. Gao CH, Yu GC, Cai P (2021) ggVennDiagram: an intuitive, easy-to-use, and highly customizable R package to generate Venn diagram. *Front Genet* 12:706907. https://doi.org/10.3389/fgene.2021.706907
34. Talevich E, Shain AH, Botton T et al (2016) CNVkit: genome-wide copy number detection and visualization from targeted DNA sequencing. *PLoS Comput Biol* 12(4):e1004873. https://doi.org/10.1371/journal.pcbi.1004873
35. Yun BG, Lee SH, Jeon JH et al (2019) Accelerated bone regeneration via three-dimensional cell-printed constructs containing human nasal turbinate-derived stem cells as a clinically applicable therapy. *ACS Biomater Sci Eng* 5(11):6171–6185. https://doi.org/10.1021/acsbiomaterials.9b01356
36. Vasiliadis AV, Galanis N (2020) Human bone marrow-derived mesenchymal stem cells from different bone sources: a panorama. *Stem Cell Investig* 7:15. https://doi.org/10.21037/sci-2020-013
37. Garcia-Contreras M, Thakor AS (2021) Human adipose tissue-derived mesenchymal stem cells and their extracellular vesicles modulate lipopolysaccharide activated human microglia. *Cell Death Discov* 7(1):98. https://doi.org/10.1038/s41420-021-00471-7
38. Choi J, Park SW, Lee H et al (2024) Human nasal inferior turbinate-derived neural stem cells improve the niche of substantia nigra par compacta in a Parkinson's disease model by modulating Hippo signaling. *Tissue Eng Regen Med* 21(5):737–748. https://doi.org/10.1007/s13770-024-00635-3
39. Lim JY, Park SI, Park SA et al (2021) Potential application of human neural crest-derived nasal turbinate stem cells for the treatment of neuropathology and impaired cognition in models of Alzheimer's disease. *Stem Cell Res Ther* 12(1):402. https://doi.org/10.1186/s13287-021-02489-1
40. Rengier F, Mehndiratta A, von Tengg-Kobligk H et al (2010) 3D printing based on imaging data: review of medical applications. *Int J CARS* 5(4):335–341. https://doi.org/10.1007/s11548-010-0476-x
41. von Poblotzki JM, Lipka T, Voss C et al (2019) Advances in manufacturing of biodegradable spinal cord implants on microscale through micromolding and 3D printing. In: 20th International Conference on Solid-State Sensors, Actuators and Microsystems & Eurosensors XXXIII (TRANSDUCERS & EUROSENSORS XXXIII), p.2185–2188. https://doi.org/10.1109/TRANSDUCERS.2019.8808647
42. Andriolo L, Reale D, Di Martino A et al (2021) Cell-free scaffolds in cartilage knee surgery: a systematic review and meta-analysis of clinical evidence. *Cartilage* 12(3):277–292. https://doi.org/10.1177/1947603519852406
43. Moore L, Cagan A, Coorens THH et al (2021) The mutational landscape of human somatic and germline cells. *Nature* 597(7876):381–386. https://doi.org/10.1038/s41586-021-03822-7
44. Biehl JK, Russell B (2009) Introduction to stem cell therapy. *J Cardiovasc Nurs* 24(2):98–103. https://doi.org/10.1097/jcn.0b013e318197a6a5
45. Wang J, Deng G, Wang S et al (2024) Enhancing regenerative medicine: the crucial role of stem cell therapy. *Front Neurosci* 18:1269577. https://doi.org/10.3389/fnins.2024.1269577
46. Kharbikar BN, Mohindra P, Desai TA (2022) Biomaterials to enhance stem cell transplantation. *Cell Stem Cell* 29(5): 692–721. https://doi.org/10.1016/j.stem.2022.04.002
47. Myers TJ, Granero-Molto F, Longobardi L et al (2010) Mesenchymal stem cells at the intersection of cell and gene therapy. *Expert Opin Biol Ther* 10(12):1663–1679. https://doi.org/10.1517/14712598.2010.531257
48. Bashor CJ, Hilton IB, Bandukwala H et al (2022) Engineering the next generation of cell-based therapeutics. *Nat Rev Drug Discov* 21(9):655–675. https://doi.org/10.1038/s41573-022-00476-6
49. Lim JY, Lee JE, Park SA et al (2022) Protective effect of human-neural-crest-derived nasal turbinate stem cells against amyloid-β neurotoxicity through inhibition of osteopontin in a human cerebral organoid model of Alzheimer's disease. *Cells* 11(6):1029. https://doi.org/10.3390/cells11061029
50. Kim H, Park K, Yon JM et al (2022) Predicting multipotency of human adult stem cells derived from various donors through deep learning. *Sci Rep* 12(1):21614. https://doi.org/10.1038/s41598-022-25423-8

51. Kim G, Jeon JH, Park K et al (2022) High throughput screening of mesenchymal stem cell lines using deep learning. *Sci Rep* 12(1):17507. https://doi.org/10.1038/s41598-022-21653-y
52. Kim DH, Kim SH, Park SH et al (2023) Characteristics of human nasal turbinate stem cells under hypoxic conditions. *Cells* 12(19):2360. https://doi.org/10.3390/cells12192360
53. Lim JY, Lee JE, Yang SH et al (2022) Development of multi-target therapy for Alzheimer's disease using human neural crest-derived stem cells. *Gerontechnology* 21:1. https://doi.org/10.4017/gt.2022.21.s.822.sp3
54. Xie Z, Gao M, Lobo AO et al (2020) 3D bioprinting in tissue engineering for medical applications: the classic and the hybrid. *Polymers* 12(8):1717. https://doi.org/10.3390/polym12081717
55. Mirshafiei M, Rashedi H, Yazdian F et al (2024) Advancements in tissue and organ 3D bioprinting: current techniques, applications, and future perspectives. *Mater Des* 240:112853. https://doi.org/10.1016/j.matdes.2024.112853
56. Paternoster JL, Vranckx JJ (2022) State of the art of clinical applications of tissue engineering in 2021. *Tissue Eng Part B Rev* 28(3):592–612. https://doi.org/10.1089/ten.teb.2021.0017
57. Tripathi S, Mandal SS, Bauri S et al (2023) 3D bioprinting and its innovative approach for biomedical applications. *MedComm* 4(1):e194. https://doi.org/10.1002/mco2.194
58. Ong CS, Yesantharao P, Huang CY et al (2018) 3D bioprinting using stem cells. *Pediatr Res* 83:223–231. https://doi.org/10.1038/pr.2017.252
59. Knight E, Przyborski S (2015) Advances in 3D cell culture technologies enabling tissue-like structures to be created *in vitro*. *J Anat* 227(6):746–756. https://doi.org/10.1111/joa.12257
60. Fang W, Yang M, Wang L et al (2023) Hydrogels for 3D bioprinting in tissue engineering and regenerative medicine: current progress and challenges. *Int J Bioprint* 9(5):759. https://doi.org/10.18063/ijb.759
61. Chen XB, Fazel Anvari-Yazdi A, Duan X et al (2023) Biomaterials/Bioinks and extrusion bioprinting. *Bioact Mater* 28:511–536. https://doi.org/10.1016/j.bioactmat.2023.06.006
62. Echeverria Molina MI, Malollari KG, Komvopoulos K (2021) Design challenges in polymeric scaffolds for tissue engineering. *Front Bioeng Biotechnol* 9:617141. https://doi.org/10.3389/fbioe.2021.617141
63. Yang BS, Liu H, Jiang LL et al (2023) 3D bioprinting of collagen-based materials for oral medicine. *Collagen Leather* 5(1):23. https://doi.org/10.1186/s42825-023-00129-3
64. Murakami J, Ishii M, Suehiro F et al (2017) Vascular endothelial growth factor-C induces osteogenic differentiation of human mesenchymal stem cells through the ERK and RUNX2 pathway. *Biochem Biophys Res Commun* 484(3):710–718. https://doi.org/10.1016/j.bbrc.2017.02.001
65. Johnson KE, Wilgus TA (2014) Vascular endothelial growth factor and angiogenesis in the regulation of cutaneous wound repair. *Adv Wound Care* 3(10):647–661. https://doi.org/10.1089/wound.2013.0517
66. Dreyer CH, Kjaergaard K, Ding M et al (2020) Vascular endothelial growth factor for in vivo bone formation: a systematic review. *J Orthop Transl* 24:46–57. https://doi.org/10.1016/j.jot.2020.05.005
67. Hölzl K, Lin S, Tytgat L et al (2016) Bioink properties before, during and after 3D bioprinting. *Biofabrication* 8(3):032002. https://doi.org/10.1088/1758-5090/8/3/032002
68. Mozafari M, Rabiee M, Azami M et al (2010) Biomimetic formation of apatite on the surface of porous gelatin/bioactive glass nanocomposite scaffolds. *Appl Surf Sci* 257(5):1740–1749. https://doi.org/10.1016/j.apsusc.2010.09.008
69. González-Sánchez M, Rivero-Antúnez P, Cumbrera-Hernández FL et al (2024) Structural and mechanical optimization of porous alumina structures fabricated by carbon sacrificial template. *J Mater Res Technol* 29:3228–3236. https://doi.org/10.1016/j.jmrt.2024.02.099
70. Lopez Reyes R, Ghim MS, Kim EC et al (2025) Hybrid modified cubic-honeycomb-plate structure: a novel bone regeneration scaffold with enhanced mechanical stiffness achieved through high printing fidelity. *J Bionic Eng* 22(4):1881–1909. https://doi.org/10.1007/s42235-025-00733-5
71. Tang GY, Liu XY, Cho M et al (2024) Pan-cancer discovery of somatic mutations from RNA sequencing data. *Commun Biol* 7: 619. https://doi.org/10.1038/s42003-024-06326-y
72. Ahmed F, Zhong J (2025) Advances in DNA/RNA sequencing and their applications in acute myeloid leukemia (AML). *Int J Mol Sci* 26(1):71. https://doi.org/10.3390/ijms26010071
73. Kaya C, Dorsaint P, Mercurio S et al (2021) Limitations of detecting genetic variants from the RNA sequencing data in tissue and fine-needle aspiration samples. *Thyroid* 31(4):589–595. https://doi.org/10.1089/thy.2020.0307
74. Suenaga H, Furukawa KS, Suzuki Y et al (2015) Bone regeneration in calvarial defects in a rat model by implantation of human bone marrow-derived mesenchymal stromal cell spheroids. *J Mater Sci Mater Med* 26(11):254. https://doi.org/10.1007/s10856-015-5591-3
75. Chamieh F, Collignon AM, Coyac BR et al (2016) Accelerated craniofacial bone regeneration through dense collagen gel scaffolds seeded with dental pulp stem cells. *Sci Rep* 6:38814. https://doi.org/10.1038/srep38814
76. Takeshita K, Motoike S, Kajiya M et al (2017) Xenotransplantation of interferon-gamma-pretreated clumps of a human mesenchymal stem cell/extracellular matrix complex induces mouse calvarial bone regeneration. *Stem Cell Res Ther* 8(1):101. https://doi.org/10.1186/s13287-017-0550-1
77. Vilaça-Faria H, Noro J, Reis RL et al (2024) Extracellular matrix-derived materials for tissue engineering and regenerative medicine: a journey from isolation to characterization and application. *Bioact Mater* 34:494–519. https://doi.org/10.1016/j.bioactmat.2024.01.004
78. Swinehart IT, Badylak SF (2016) Extracellular matrix bioscaffolds in tissue remodeling and morphogenesis. *Dev Dyn* 245(3): 351–360. https://doi.org/10.1002/dvdy.24379
79. Cox TR, Erler JT (2011) Remodeling and homeostasis of the extracellular matrix: implications for fibrotic diseases and cancer. *Dis Model Mech* 4(2):165–178. https://doi.org/10.1242/dmm.004077
80. Bonnans C, Chou J, Werb Z (2014) Remodelling the extracellular matrix in development and disease. *Nat Rev Mol Cell Biol* 15(12):786–801. https://doi.org/10.1038/nrm3904
81. Winkler J, Abisoye-Ogunniyan A, Metcalf KJ et al (2020) Concepts of extracellular matrix remodelling in tumour progression and metastasis. *Nat Commun* 11:5120. https://doi.org/10.1038/s41467-020-18794-x
82. Yan LF, Wang J, Cai X et al (2024) Macrophage plasticity: signaling pathways, tissue repair, and regeneration. *MedComm*

5(8):e658.
https://doi.org/10.1002/mco2.658
83. Witherel CE, Sao K, Brisson BK et al (2021) Regulation of extracellular matrix assembly and structure by hybrid M1/M2 macrophages. *Biomaterials* 269:120667.
https://doi.org/10.1016/j.biomaterials.2021.120667
84. Yang H, Cheng H, Dai R et al (2023) Macrophage polarization in tissue fibrosis. *PeerJ* 11:e16092.
https://doi.org/10.7717/peerj.16092
85. Li M, Hou Q, Zhong L et al (2021) Macrophage related chronic inflammation in non-healing wounds. *Front Immunol* 12:681710.
https://doi.org/10.3389/fimmu.2021.681710
86. Bakhtina A, Tohfafarosh M, Lichtler A et al (2014) Characterization and differentiation potential of rabbit mesenchymal stem cells for translational regenerative medicine. *In Vitro Cell Dev Biol Anim* 50(3):251–260.
https://doi.org/10.1007/s11626-013-9702-5
87. Lee TC, Lee TH, Huang YH et al (2014) Comparison of surface markers between human and rabbit mesenchymal stem cells. *PLoS ONE* 9(11):e111390.
https://doi.org/10.1371/journal.pone.0111390
88. Zomer HD, Roballo KC, Lessa TB et al (2018) Distinct features of rabbit and human adipose-derived mesenchymal stem cells: implications for biotechnology and translational research. *Stem Cells Cloning* 11:43–54.
https://doi.org/10.2147/sccaa.s175749
89. Blanco JF, García-Briñon J, Benito-Garzón L et al (2018) Human bone marrow mesenchymal stromal cells promote bone regeneration in a xenogeneic rabbit model: a preclinical study. *Stem Cells Int* 2018:7089484.
https://doi.org/10.1155/2018/7089484
90. Svensson B, Nagubothu SR, Cedervall J et al (2011) Injection of human mesenchymal stem cells improves healing of vocal folds after scar excision: a xenograft analysis. *Laryngoscope* 121(10):2185–2190.
https://doi.org/10.1002/lary.22143
91. Niemeyer P, Szalay K, Luginbühl R et al (2010) Transplantation of human mesenchymal stem cells in a non-autogenous setting for bone regeneration in a rabbit critical-size defect model. *Acta Biomater* 6(3):900–908.
https://doi.org/10.1016/j.actbio.2009.09.007
92. Bracey DN, Cignetti NE, Jinnah AH et al (2020) Bone xenotransplantation: a review of the history, orthopedic clinical literature, and a single-center case series. *Xenotransplantation* 27(5):e12600.
https://doi.org/10.1111/xen.12600
93. Maacha S, Sidahmed H, Jacob S et al (2020) Paracrine mechanisms of mesenchymal stromal cells in angiogenesis. *Stem Cells Int* 2020(1):4356359.
https://doi.org/10.1155/2020/4356359
94. Johnson GA, Burghardt RC, Bazer FW et al (2003) Osteopontin: roles in implantation and placentation. *Biol Reprod* 69(5):1458–1471.
https://doi.org/10.1095/biolreprod.103.020651
95. Bai RJ, Li YS, Zhang FJ (2022) Osteopontin, a bridge links osteoarthritis and osteoporosis. *Front Endocrinol* 13:1012508.
https://doi.org/10.3389/fendo.2022.1012508
96. Vancea A, Serban O, Fodor D (2021) Relationship between osteopontin and bone mineral density. *Acta Endo (Buc)* 17(4):509–516.
https://doi.org/10.4183/aeb.2021.509
97. Si JY, Wang CW, Zhang DH et al (2020) Osteopontin in bone metabolism and bone diseases. *Med Sci Monit* 26:e919159.
https://doi.org/10.12659/msm.919159
98. Komori T (2002) Runx2, a multifunctional transcription factor in skeletal development. *J Cell Biochem* 87(1):1–8.
https://doi.org/10.1002/jcb.10276
99. Qin X, Jiang Q, Nagano K et al (2020) Runx2 is essential for the transdifferentiation of chondrocytes into osteoblasts. *PLoS Genet* 16(11):e1009169.
https://doi.org/10.1371/journal.pgen.1009169
100. Qin X, Jiang Q, Matsuo Y et al (2015) Cbfb regulates bone development by stabilizing Runx family proteins. *J Bone Miner Res* 30(4):706–714.
https://doi.org/10.1002/jbmr.2379
101. Komori T (2020) Molecular mechanism of Runx2-dependent bone development. *Mol Cells* 43(2):168–175